



## **ALMA Lensing Cluster Survey: Hubble Space Telescope and Spitzer Photometry of 33 Lensed Fields Built with CHArGE**

Downloaded from: <https://research.chalmers.se>, 2023-01-21 00:55 UTC

Citation for the original published paper (version of record):

Kokorev, V., Brammer, G., Fujimoto, S. et al (2022). ALMA Lensing Cluster Survey: Hubble Space Telescope and Spitzer Photometry of 33 Lensed Fields Built with CHArGE. *Astrophysical Journal, Supplement Series*, 263(2).  
<http://dx.doi.org/10.3847/1538-4365/ac9909>

N.B. When citing this work, cite the original published paper.



# ALMA Lensing Cluster Survey: Hubble Space Telescope and Spitzer Photometry of 33 Lensed Fields Built with CHARGE

V. Kokorev<sup>1,2</sup> , G. Brammer<sup>1,2</sup> , S. Fujimoto<sup>1,2</sup> , K. Kohno<sup>3,4</sup> , G. E. Magdis<sup>1,2,5</sup> , F. Valentino<sup>1,2</sup> , S. Toft<sup>1,2,5</sup> , P. Oesch<sup>1,6</sup> , I. Davidzon<sup>1,2</sup> , F. E. Bauer<sup>7,8,9</sup> , D. Coe<sup>10</sup> , E. Egami<sup>11</sup> , M. Oguri<sup>4,12,13</sup> , M. Ouchi<sup>13,14,15</sup> , M. Postman<sup>10</sup> , J. Richard<sup>16</sup> , J.-B. Jolly<sup>17,18</sup> , K. K. Knudsen<sup>17</sup> , F. Sun<sup>11</sup> , J. R. Weaver<sup>1,19</sup> , Y. Ao<sup>20,21</sup> , A. J. Baker<sup>22,23</sup> , L. Bradley<sup>10</sup> , K. I. Caputi<sup>1,24</sup> , M. Dessauges-Zavadsky<sup>25</sup> , D. Espada<sup>26,27</sup> , B. Hatsukade<sup>3</sup> , A. M. Koekemoer<sup>10</sup> , A. M. Muñoz Arancibia<sup>28,29</sup> , K. Shimasaku<sup>4,30</sup> , H. Umehata<sup>31,32</sup> , T. Wang<sup>33</sup> , and W.-H. Wang<sup>34</sup>

<sup>1</sup> Cosmic Dawn Center (DAWN), Jagtvej 128, DK-2200 Copenhagen N, Denmark

<sup>2</sup> Niels Bohr Institute, University of Copenhagen, Blegdamsvej 17, DK-2100 Copenhagen Ø, Denmark; [vasilii.kokorev@nbi.ku.dk](mailto:vasilii.kokorev@nbi.ku.dk)

<sup>3</sup> Institute of Astronomy, Graduate School of Science, The University of Tokyo, 2-21-1 Osawa, Mitaka, Tokyo, 181-0015, Japan

<sup>4</sup> Research Center for the Early Universe, Graduate School of Science, The University of Tokyo, 7-3-1 Hongo, Bunkyo-ku, Tokyo, 113-0033, Japan

<sup>5</sup> DTU-Space, Technical University of Denmark, Elektrovej 327, DK-2800 Kgs. Lyngby, Denmark

<sup>6</sup> Department of Astronomy, University of Geneva, Chemin Pegasi 51, 1290 Versoix, Switzerland

<sup>7</sup> Instituto de Astrofísica, Facultad de Física, Pontificia Universidad Católica de Chile, Campus San Joaquín, Av. Vicuña Mackenna 4860, Macul Santiago, 7820436, Chile

<sup>8</sup> Centro de Astroingeniería, Facultad de Física, Pontificia Universidad Católica de Chile, Campus San Joaquín, Av. Vicuña Mackenna 4860, Macul Santiago, 7820436, Chile

<sup>9</sup> Millennium Institute of Astrophysics, Nuncio Monseñor Sótero Sanz 100, Of 104, Providencia, Santiago, Chile

<sup>10</sup> Space Telescope Science Institute, 3700 San Martin Drive, Baltimore, MD 21218, USA

<sup>11</sup> Steward Observatory, University of Arizona, 933 N. Cherry Avenue, Tucson, AZ 85721, USA

<sup>12</sup> Center for Frontier Science, Chiba University, 1-33 Yayoi-cho, Inage-ku, Chiba, 263-8522, Japan

<sup>13</sup> Kavli Institute for the Physics and Mathematics of the Universe (WPI), The University of Tokyo, 5-1-5 Kashiwanoha, Kashiwa-shi, Chiba, 277-8583, Japan

<sup>14</sup> National Astronomical Observatory of Japan, 2-21-1 Osawa, Mitaka, Tokyo, 181-8588, Japan

<sup>15</sup> Institute for Cosmic Ray Research, The University of Tokyo, 5-1-5 Kashiwanoha, Kashiwa, Chiba, 277-8582, Japan

<sup>16</sup> Univ Lyon, Univ Lyon1, Ens de Lyon, CNRS, Centre de Recherche Astrophysique de Lyon UMR5574, F-69230 Saint-Genis-Laval, France

<sup>17</sup> Department of Space, Earth and Environment, Chalmers University of Technology, Onsala Space Observatory, SE-439 92 Onsala, Sweden

<sup>18</sup> Max-Planck-Institut für extraterrestrische Physik, D-85748 Garching, Germany

<sup>19</sup> Department of Astronomy, University of Massachusetts, Amherst, MA 01003, USA

<sup>20</sup> Purple Mountain Observatory and Key Laboratory for Radio Astronomy, Chinese Academy of Sciences, Nanjing, People's Republic of China

<sup>21</sup> School of Astronomy and Space Science, University of Science and Technology of China, Hefei, People's Republic of China

<sup>22</sup> Department of Physics and Astronomy, Rutgers, the State University of New Jersey, 136 Frelinghuysen Road, Piscataway, NJ 08854-8019, USA

<sup>23</sup> Department of Physics and Astronomy, University of the Western Cape, Robert Sobukwe Road, Bellville 7535, South Africa

<sup>24</sup> Kapteyn Astronomical Institute, University of Groningen, P.O. Box 800, 9700AV Groningen, The Netherlands

<sup>25</sup> Observatoire de Genève, Université de Genève, Versoix, Switzerland

<sup>26</sup> Departamento de Física Teórica y del Cosmos, Campus de Fuentenueva, Edificio Mecenas, Universidad de Granada, E-18071, Granada, Spain

<sup>27</sup> Instituto Carlos I de Física Teórica y Computacional, Facultad de Ciencias, E-18071, Granada, Spain

<sup>28</sup> Millennium Institute of Astrophysics (MAS), Nuncio Monseñor Sótero Sanz 100, Providencia, Santiago, Chile

<sup>29</sup> Center for Mathematical Modeling, Universidad de Chile, Beauchef 851, Santiago 8320000, Chile

<sup>30</sup> Department of Astronomy, Graduate School of Science, The University of Tokyo, 7-3-1 Hongo, Bunkyo-ku, Tokyo, 113-0033, Japan

<sup>31</sup> Institute for Advanced Research, Nagoya University, Furocho, Chikusa, Nagoya, 464-8602, Japan

<sup>32</sup> Department of Physics, Graduate School of Science, Nagoya University, Furocho, Chikusa, Nagoya, 464-8602, Japan

<sup>33</sup> Key Laboratory of Modern Astronomy and Astrophysics (Nanjing University), Ministry of Education, Nanjing 210093, People's Republic of China

<sup>34</sup> Institute of Astronomy and Astrophysics, Academia Sinica, No 1, Sec 4, Roosevelt Rd., Taipei City, 10617, Taiwan

Received 2022 July 18; revised 2022 September 16; accepted 2022 October 5; published 2022 December 7

## Abstract

We present a set of multiwavelength mosaics and photometric catalogs in the Atacama Large Millimeter/submillimeter Array (ALMA) lensing cluster survey fields. The catalogs were built by the reprocessing of archival data from the Complete Hubble Archive for Galaxy Evolution compilation, taken by the Hubble Space Telescope (HST) in the Reionization Lensing Cluster Survey, Cluster Lensing And Supernova survey with Hubble, and Hubble Frontier Fields. Additionally, we have reconstructed the Spitzer Infrared Array Camera 3.6 and 4.5  $\mu\text{m}$  mosaics, by utilizing all the available archival IPAC Infrared Science Archive/Spitzer Heritage Archive exposures. To alleviate the effect of blending in such a crowded region, we have modeled the Spitzer photometry by convolving the HST detection image with the Spitzer point-spread function using the novel GOLFIR software. The final catalogs contain 218,000 sources, covering a combined area of 690 arcmin<sup>2</sup>, a factor of  $\sim 2$  improvement over the currently existing photometry. A large number of detected sources is a result of reprocessing of all available and sometimes deeper exposures, in conjunction with a combined optical–near-IR detection strategy. These data will serve as an important tool in aiding the search of the submillimeter galaxies in future ALMA surveys, as well as follow-ups of the HST dark and high- $z$  sources with JWST. Coupled with the available HST photometry, the



Original content from this work may be used under the terms of the [Creative Commons Attribution 4.0 licence](https://creativecommons.org/licenses/by/4.0/). Any further distribution of this work must maintain attribution to the author(s) and the title of the work, journal citation and DOI.

addition of the 3.6 and 4.5  $\mu\text{m}$  bands will allow us to place a better constraint on the photometric redshifts and stellar masses of these objects, thus giving us an opportunity to identify high-redshift candidates for spectroscopic follow-ups and to answer the important questions regarding the Epoch of Reionization and formation of the first galaxies. The mosaics, photometric catalogs, and the best-fit physical properties are publicly available at <https://github.com/dawn-cph/alcs-clusters>.

*Unified Astronomy Thesaurus concepts:* [Galaxy evolution \(594\)](#); [Catalogs \(205\)](#); [High-redshift galaxies \(734\)](#); [Interstellar medium \(847\)](#); [Submillimeter astronomy \(1647\)](#); [Photometry \(1234\)](#)

## 1. Introduction

The emergence of large, multiwavelength photometric surveys has allowed us to conduct detailed studies of galaxy formation and evolution across cosmic time by observing a statistically significant population of galaxies. In particular, the investment of thousands of orbits of Hubble Space Telescope (HST) and Spitzer Space Telescope (Spitzer) time has cemented their unprecedented imaging legacy and enabled us to revolutionize our understanding of both observational cosmology and galaxy evolution. For example, these unique capabilities allowed us to capture the accelerating expansion of the universe (Riess et al. 2004), and have helped demonstrate that the majority of star formation took place within a relatively short time span, in the epoch at  $1 < z < 3$  (see, e.g., Hopkins & Beacom 2006; Bouwens et al. 2007).

More recently, the advantages of space-based observations have become particularly pronounced in the search for high-redshift galaxies, with the combined efforts of the very-sensitive Wide Field Camera 3 (WFC3) on board HST and the ultradeep Spitzer Infrared Array Camera (IRAC) imaging. The remarkable wavelength coverage of these instruments has helped us push the observational frontier to the end of the cosmic Epoch of Reionization at  $z \sim 7\text{--}8$ , some 700 Myr from the Big Bang, and toward the epoch beyond  $z \sim 10$ , where the formation of the first galaxies has taken place. A number of large, deep extragalactic blank field surveys has now led to the discovery of a significant and statistically meaningful number of galaxies at  $z \sim 7\text{--}8$  (e.g., McLure et al. 2013; Bouwens et al. 2015; Finkelstein et al. 2015), an ever-growing sample of  $z \sim 9\text{--}11$  candidates (Ellis et al. 2013; Oesch et al. 2013, 2014; Bouwens et al. 2016; Calvi et al. 2016), and even the most distant galaxy discovered to date, at  $z = 11.1$  (Oesch et al. 2016; Jiang et al. 2021). The most staggering and impactful discoveries of high- $z$  galaxies have, however, been made within lensing cluster fields, which include the Hubble Frontier Fields (HFF; Lotz et al. 2017), the Reionization Lensing Cluster Survey (RELICS; Coe et al. 2019), and the Cluster Lensing And Supernova survey with Hubble (CLASH; Postman et al. 2012). All three combine the power of HST and Spitzer observations and a strong gravitational lensing potential of massive galaxy clusters to produce the deepest available observations of high- $z$  galaxies lensed by clusters ever obtained (see, e.g., Zheng et al. 2012; Coe et al. 2013; Bradley et al. 2014; Schmidt et al. 2014; Zitrin et al. 2014; Infante et al. 2015; Ishigaki et al. 2015; Kawamata et al. 2015; McLeod et al. 2015; Oesch et al. 2015; Hashimoto et al. 2018; Hoag et al. 2018; Strait et al. 2020).

The redshift estimates of these objects still largely rely on spectral energy distribution (SED) fitting of broadband photometry, and spectroscopically confirmed samples remain limited. The SED fitting photometric redshift technique is largely leveraged on the correct identifications of either the Lyman or Balmer breaks, at 912 Å and 3640 Å, respectively, in

the stellar continuum. At  $z \sim 9\text{--}10$  the Spitzer/IRAC targets the  $\sim 3000\text{--}4000$  Å rest-frame continuum and, as such, can greatly aid in removing the low-redshift interlopers from the high- $z$  samples. Moreover, even for spectroscopically confirmed objects the Spitzer observations are essential for conducting robust measurements of the stellar population parameters, such as stellar mass ( $M_*$ ), dust-attenuated star formation rate (SFR), and extinction ( $A_V$ ) (González et al. 2011; Ryan et al. 2014; Salmon et al. 2015). The existing data have already led to implications that the first main episodes of star formation took place  $\sim 250$  Myr after the Big Bang (Hashimoto et al. 2018).

Some questions regarding star formation, however, are yet to be answered. The rest-frame UV and far-IR (FIR) observations conducted during the last decade (Le Floch et al. 2005, 2009), present us with a view of the universe where the star formation has already reached its peak at  $z \sim 2\text{--}3$  and is now declining (e.g., Madau & Dickinson 2014; Zavala et al. 2021). Studies of the SFR density (SFRD) also show a growing disparity between the contribution of dust-obscured SFRs, measured from IR data, and unobscured SFRs, measured from UV–optical data. This, in return, might imply that the early universe was less dusty, aligning with some of our predictions regarding the timescale and mechanisms of dust production. On the other hand, blind Atacama Large Millimeter/submillimeter Array (ALMA) studies of galaxies at  $z \sim 2\text{--}6$  (Wang et al. 2016, 2019; Yamaguchi et al. 2019; Gruppioni et al. 2020; Umehata et al. 2020; Manning et al. 2022; Sun et al. 2022) reveal a population of optically dark, dusty sources, which contribute 10 times more toward the SFRD than similarly bright galaxies with a rest-frame UV detection, and reside within centers of the most massive overdensities (Zhou et al. 2021). The ubiquity of such systems can potentially create obstacles in our understanding of the true numbers of massive galaxies, the SFRD in the early universe, and challenge our current understanding of galaxy formation. As a result, our ability to correctly recover the total SFR comes down to the detection of high- $z$  dusty galaxies, such as “HST dark” or optically dark sources.

The complete dust obscuration of UV–optical emission makes the detection and identification of these objects a significant challenge, even when sufficient mid-IR and FIR coverage are available. As a result, the only reliable way to observe such objects are blind field studies with ALMA or the Northern Extended Millimeter Array (NOEMA). ALMA, in particular, has been the primary tool driving the discovery of new faint submillimeter galaxies, ( $S_{1.2\text{mm}} \sim 0.02\text{--}1$  mJy), which are substantially fainter compared to the traditionally observed submillimeter galaxies (SMGs; see, e.g., Hatsukade et al. 2013; Ono et al. 2014; Carniani et al. 2015; Aravena et al. 2016; Fujimoto et al. 2016; Hatsukade et al. 2016; Oteo et al. 2016; Dunlop et al. 2017; González-López et al. 2017; Franco et al. 2018; Sun et al. 2022). Over the last few years, ALMA

observations of faint 1.2 mm sources have been able to derive ALMA millimeter counts down to depths of  $\sim 0.02$  mJy (Carniani et al. 2015; Aravena et al. 2016; Fujimoto et al. 2016; Hatsukade et al. 2016); however, despite such depths, the origin of the cosmic infrared background (CIB), and therefore the majority of SFRDs, still remains hidden. It has quickly become apparent that deeper ALMA observations are absolutely imperative in order to separate and resolve the remainder of the CIB into discrete sources, in order to study their individual properties. The most efficient way to complete this puzzle is to observe a sufficiently large number of lensing clusters using ALMA.

The ALMA Lensing Cluster Survey (ALCS; Project ID: 2018.1.00035.L; PI: K. Kohno) aims to do exactly that. At the moment, it is the largest, by area, among other ALMA surveys targeting clusters of galaxies. Combined with previous ALMA observations, the survey covers a total of 33 massive galaxy clusters. The observations aim to provide an in-depth look of the high-magnification regions within the cluster fields, and, in particular, target dust-continuum-selected and line-emitting high- $z$  galaxies. The main science goal of the survey is to examine the faint-end slope of the 1.2 mm source counts and to provide the best estimate for the CIB at that wavelength. The typical galaxies contributing to the CIB at 1.2 mm are intrinsically faint (see, e.g., Fujimoto et al. 2016); however, in conjunction with the rich HST and Spitzer/IRAC data sets covering the field, the survey aims to reveal the fundamental physical properties of the  $S_{1.2\text{ mm}} < 0.1$  mJy galaxies, such as their stellar masses and IR-based SFRs (see Sun et al. 2022).

All ALCS clusters have been previously imaged with the HST and Spitzer/IRAC, enabling accurate positions and other quantities derived from the photometry. In this work we describe the reprocessing of all archival HST and Spitzer/IRAC mosaics covering the ALCS. We perform careful aperture photometry of all HST sources, and use them as priors to model and fit the flux densities for the sources in the blended IRAC maps. The final images and catalogs will then act as a powerful tool to establish better constraints on the photometric redshifts and physical properties of these objects. In addition, this allows us to identify high-redshift candidates for spectroscopic follow-ups and answer the important questions regarding the Epoch of Reionization and formation of first galaxies.

The provided catalogs include HST and Spitzer photometry, photometric redshifts, and stellar population properties, for each field included in the ALCS, similarly to the ASTRODEEP collaboration (Merlin et al. 2016a; Di Criscienzo et al. 2017) and the HFF-DeepSpace catalogs (Shiple et al. 2018), albeit following a different methodology. Moreover, the public release of our data is complemented by all the new HST/Advanced Camera for Surveys (ACS), HST/WFC3, and IRAC mosaics, including detection images, models, residuals, and segmentation maps.

The paper is organized as follows. In Section 2 we list the data sets used in this work, and describe the creation of new Spitzer/IRAC mosaics. In Section 3 we describe the high- and low-resolution photometry algorithms. In Section 4 we describe the catalog format, ALMA counterparts, and quality flags, and present a quality and consistency check for our catalog. In Section 5 we describe the SED fitting of our photometry, resultant photometric redshifts, stellar population parameters,

and rest-frame colors. Finally, our main conclusions and summary are given in Section 6.

Throughout this paper we assume a flat  $\Lambda$ CDM cosmology, with  $\Omega_{m,0} = 0.3$ ,  $\Omega_{\Lambda,0} = 0.7$ , and  $H_0 = 70$  km s $^{-1}$  Mpc $^{-1}$ , and a Chabrier (2003) initial mass function. All magnitudes in this paper are expressed in the AB system (Oke 1974), for which a flux  $f_\nu$  in jansky ( $10^{-23}$  erg cm $^{-2}$  s $^{-1}$  Hz $^{-1}$ ) corresponds to  $AB = 23.9 - 2.5 \log_{10}(f_\nu/\mu\text{Jy})$ .

## 2. Data Sets

The ALCS is a Cycle 6 ALMA large program targeting 33 lensing cluster fields in Band 6 ( $\bar{\lambda} = 1.15$  mm/ $\bar{\nu} = 260$  GHz). In total the ALCS covers an area of 134 arcmin $^2$ , with synthesized beam response smaller than  $0''.5$ , reaching a depth of 70  $\mu\text{Jy}$  ( $1\sigma$ ). The sample is designed to be contained within the best-studied massive clusters also imaged in HST programs. More specifically, the ALCS includes five clusters from HFF (Lotz et al. 2017), plus the new BUFFALO observations (Steinhardt et al. 2020), 16 clusters from the RELICS (Coe et al. 2019), and 12 clusters from CLASH (Postman et al. 2012).

We list a few major motivations in constructing uniform HST/Spitzer mosaics in ALCS fields as follows. The vast majority of objects within the ALCS are only continuum detected, ruling out redshift constraints from spectra. However, the rich UV–optical and near-IR (NIR) treasury data already collected within these cluster fields will allow for the derivation of photometric redshifts for a vast majority of faint SMGs. This will allow the derivation of the dust-based FIR luminosity functions, and give upper limits on its evolution at  $z > 3$ , something that has been out of reach for Spitzer and Herschel.

The ALCS is also expected to detect the ionized carbon ([C II]) and carbon monoxide (CO) emission lines, facilitating studies of the interstellar medium (ISM) for a unique sample of faint galaxies magnified by lensing clusters. Moreover, even for nondetections the millimeter-wave properties of various classes of star-forming galaxies can be extracted through stacking, facilitated by the presence of both HST and IRAC priors within these lensed fields (see, e.g., A. Guerrero et al. 2022, in preparation, and J. B. Jolly et al. 2022, in preparation).

An additional emphasis of the survey is to detect and characterize the magnified ALMA continuum sources, without HST counterparts, i.e., the intrinsically faint, ‘‘HST dark’’ ALMA sources. The majority of these objects also have faint counterparts in the Spitzer/IRAC bands, with the measured IRAC to 1.2 mm flux density ratios (Sun et al. 2022) pointing toward these sources being either distant  $z \gtrsim 4$  galaxies, or massive brightest cluster galaxy (BCG) progenitors at  $z \sim 4$ , similar to the objects presented in Wang et al. (2016, 2019), Yamaguchi et al. (2019), Gruppioni et al. (2020), and Umehata et al. (2020).

### 2.1. CHArGE Hubble Space Telescope Imaging

The Complete Hubble Archive for Galaxy Evolution (CHArGE) is a novel initiative that performs uniform processing of all archival HST imaging and slitless spectroscopy observations relevant for studying distant galaxies (e.g., reasonably high galactic latitudes, avoiding large foreground galaxies, including WFC3/IR). The data were processed with the GRIZLI pipeline (Brammer & Matharu 2021), which creates filter mosaics for all ACS, WFC3/UVIS, and WFC3/IR

exposures that cover a given area of the sky (e.g., an ALCS field). It is worth noting that the produced catalogs span, for each cluster, an area multiple times larger than that of the ALCS ALMA maps. The overlapping exposures are then broken into discrete “visit” associations, where the grouping is done for a given filter for data that were taken in a single target acquisition. These associations generally share the same spacecraft orientation and zodiacal sky background.

Within a single visit, all exposures are aligned to each other using high signal-to-noise ratio (S/N) sources detected in them, allowing the relative  $x$  and  $y$  coordinates between exposures to shift until the best match is found. These are analogous to `DrizzlePac TweakShifts` and are generally a fairly small fraction of a pixel for dither offsets within a single orbit and a few tenths of a pixel between subsequent orbits that share the same initial target acquisition.

A source catalog is created from a preliminary mosaic generated from the visit exposures and aligned (shift, rotation, scale) to an astrometric reference catalog. Generally this is PanSTARRS Data Release 1 (Flewelling et al. 2020), as it is well aligned to the Gaia Data Release 2 (DR2; Gaia Collaboration et al. 2016, 2018) but has a higher source density than the bright Gaia stars alone.

The final fine alignment is performed simultaneously optimizing (a) the alignment between all individual visit catalogs, and (b) Gaia DR2 stars with proper motions projected to each visit observation epoch. This ensures robust internal alignment of the HST images for matched-aperture photometry, and the final absolute astrometric precision is generally  $<100$  mas.

A pedestal sky background of each exposure is estimated in the `AstroDrizzle` preparation of each visit association. A smooth background is subtracted from each visit mosaic to remove gradients that can then appear as sharp discontinuities in the final combined filter mosaics. This background is estimated with `SEP` (Barbary 2016), a PYTHON implementation of `SOURCEEXTRACTOR` (Bertin & Arnouts 1996) with `BACK_FILTERSIZE=3` and `BACK_SIZE=32''`. While the background estimation includes a mask for detected sources, it can include extended structure for very large, bright galaxies and intercluster light (ICL) in the ALCS cluster fields.

Final rectified mosaics combining all exposures in each available filter are created with `AstroDrizzle`. All WFC3/IR mosaics are created with  $0''.1$  pixels, while the ACS and UVIS optical/UV images are drizzled with  $0''.05$  pixels on a grid that subsamples the IR mosaic  $2 \times 2$ . Both optical/UV and IR mosaics are drizzled with `pixfrac=0.33`. The `sci` (science) and `wht` (inverse variance weights) mosaics are provided for each filter.

While this approach might not necessarily result in the best reconstruction of the undersampled HST point-spread functions (PSFs), the larger pixels ensure more uniform weights across the diversity of dither coverage across the survey fields (e.g., hundreds of exposures for the Frontier Fields but as few as 2–4 exposures for some pre-RELICS filters). The larger pixels and small `pixfrac` result in lower correlated noise between adjacent pixels, and therefore the inverse variance maps are a more reliable estimate of the pixel variances for, e.g., aperture photometry.

The units of the filter mosaics are in electrons  $s^{-1}$ , with the photometric calibration to cgs units provided in the `PHOTFLAM` ( $f_\lambda$ ) and `PHOTFNU` ( $f_\nu$ ) header keywords of each mosaic. We

additionally provide PSF models for each IR filter using the effective PSF models described in Anderson & King (2000). The sources of all HST data used for this work are listed in Appendix A.

## 2.2. Infrared Array Camera Imaging

We begin by collecting all the Basic Calibrated Data (BCD) exposures (pBCD), from the Spitzer Heritage Archive for each field in the ALCS. These include IRAC exposures in Spitzer Frontier Fields/HFF (Lotz et al. 2019), the Spitzer Reionization Lensing Cluster Survey/RELICS (Bradac et al. 2020), and CLASH (CLASH Team 2020). Our Spitzer data only include Spitzer/IRAC 3.6 and  $4.5 \mu\text{m}$ , as our fields of interest do not have a uniform coverage in  $5.8$  and  $8 \mu\text{m}$ . Similarly to how we process the HST CHARGE data, we perform relative alignment of all exposures in the IRAC Astronomical Observation Requests (AORs), and then align AOR mosaics to Gaia DR2. A larger size of IRAC field of view is generally beneficial, as it allows for a sufficient number of reference sources to be used for alignment.

The IRAC background is removed by creating a master background image for each AOR with detected sources masked. Finally, the complete IRAC mosaics are aligned to the HST pixel grid and drizzled with  $0''.5$  pixels and the pixel fraction parameter `pixfrac` set to 0.2. With full knowledge of the individual pBCD exposures that contribute at any location in the final mosaic, we can generate robust models of the IRAC PSF that fully account for the diversity of depth and detector position angle across the mosaic. These position-dependent PSFs are used for the IRAC model-based photometry, and can be regenerated using `GOLFIR` (Brammer 2022).

## 3. Photometry

During the generation of this catalog, we treated the highly resolved (HST/ACS and WFC3) data differently from the low-resolution Spitzer/IRAC data. In Figure 1 we show footprints for all the available HST and Spitzer photometry in four Frontier Fields. We additionally highlight the area covered by the ALCS. An array of filter response curves for all available bands is presented in Figure 2.

### 3.1. Source Detection

The survey fields studied here are crowded with galaxy cluster members and diffuse intracluster light that present a challenge for robust isolation and detection of sources, including both cluster members and stars and galaxies in the foreground and background of the clusters. To cover the large dynamic range of brightness and physical size of sources in the field, we adopt a hybrid source-detection approach somewhat similar to the wavelet decomposition developed by Livermore et al. (2017). We first create a master detection image,  $D$ , that is a combination of the ACS F814W and WFC3 F105W, F125W, F140W, and F160W mosaics weighted by the inverse variance maps of each. Then we create two median-filtered versions of the detection image,  $M_{16}$  and  $M_{48}$ , filtered on scales of 16 and 48 pixels ( $1''.6$  and  $4''.8$ ), respectively. The brightest, most extended sources are detected on the most smoothed image,  $M_{48}$ , with the `SEP` source-detection software (Barbary 2016). Intermediate sources are detected on the  $M_{16}$ – $M_{48}$  filtered image, and a final detection is run on the  $D$ – $M_{16}$  image where all but the

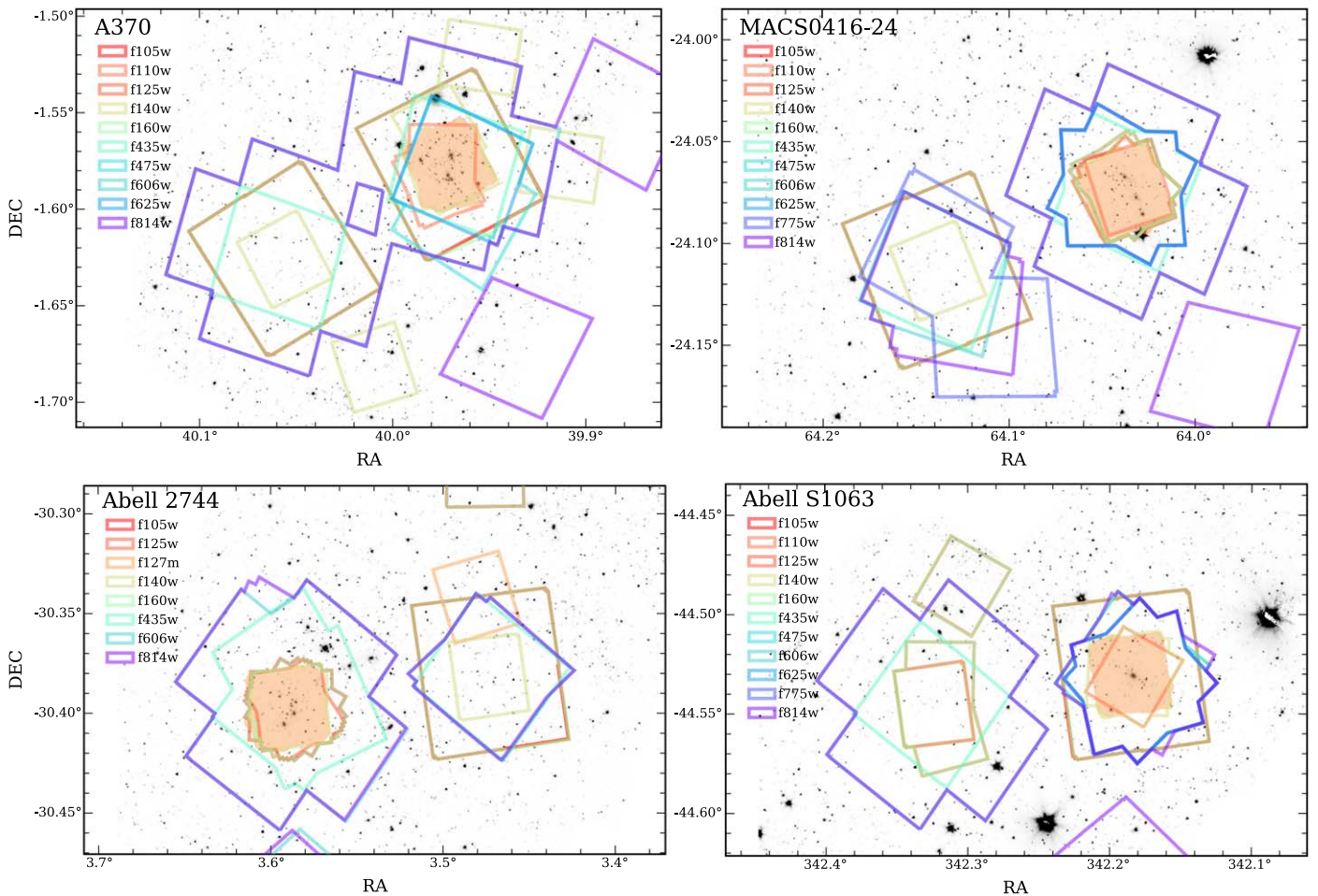


**Figure 1.** Footprint of the HST observations, superimposed on the Spitzer/IRAC  $3.6\ \mu\text{m}$  data of four Frontier Fields clusters (Lotz et al. 2017). The ALCS band 6 ALMA coverage is shown as the shaded orange areas. The images shown cover both the cluster and the parallels of the HFF.

most compact features have been filtered out. The final list of detected sources is the union of these three layers after removing duplicates between them.

### 3.2. Hubble Space Telescope Photometry

We extract aperture photometry within (circular) aperture diameters  $0''.36$ ,  $0''.5$ ,  $0''.7$ ,  $1''.0$ ,  $1''.2$ ,  $1''.5$ ,  $3''.0$  at the positions derived in the source detection as described above. We do not perform PSF-matching for any HST filters for the aperture measurements. This PSF-matching approach is quite common in the literature (see, e.g., Shipley et al. 2018), however performing it on the images can result in substantial deleterious effects on the noise properties of the derived photometry at shorter wavelengths. In particular, faint and/or dropout sources would be most affected, where there is no signal to use in matching. In this work our scope is to focus on the faint, marginally detected objects. While the PSF-matching approach would result in, generally, more robust colors and photometric redshifts, we favor the approach here, primarily for simplicity and consistency across a wide variety of fields, with different noise properties, and defer tests on the aperture effects to ongoing work. Together with the derived photometry we also provide HST mosaics for all filters, which can be utilized to perform the PSF-matched photometry extraction if necessary.

To compute aperture corrections we have defined the “total” HST flux density within an elliptical Kron aperture determined by SEP, as in SOURCEEXTRACTOR. However, we do not impose the lower limit of 3.5 on KRON\_RADIUS typical with SOURCEEXTRACTOR as we find that in fact most derived values are actually lower than this threshold even for bright, well-measured sources. We do, however, impose a minimum circularized Kron aperture diameter of  $0''.7$ , which is our favored “color” aperture. We calculate a correction for flux outside of the Kron aperture using the PSF curves of growth (i.e., explicitly valid only for point sources). The “color” aperture fluxes are therefore corrected by (1)  $\text{flux\_auto}/\text{flux\_aper}$  in the detection band and then (2) by the Kron aperture correction.

### 3.3. Infrared Array Camera Photometry

Calculating the photometry from low-resolution data, particularly in crowded regions containing galaxy clusters, can be a difficult technical challenge. In order to correctly extract the flux density in the redder bands, the significant differences that exist between the HST data and the much lower resolution Spitzer/IRAC image data must be taken into account. Primarily this concerns the problem of blending, wherein a standard aperture photometry approach normally used for high-resolution data would be inadequate. To tackle

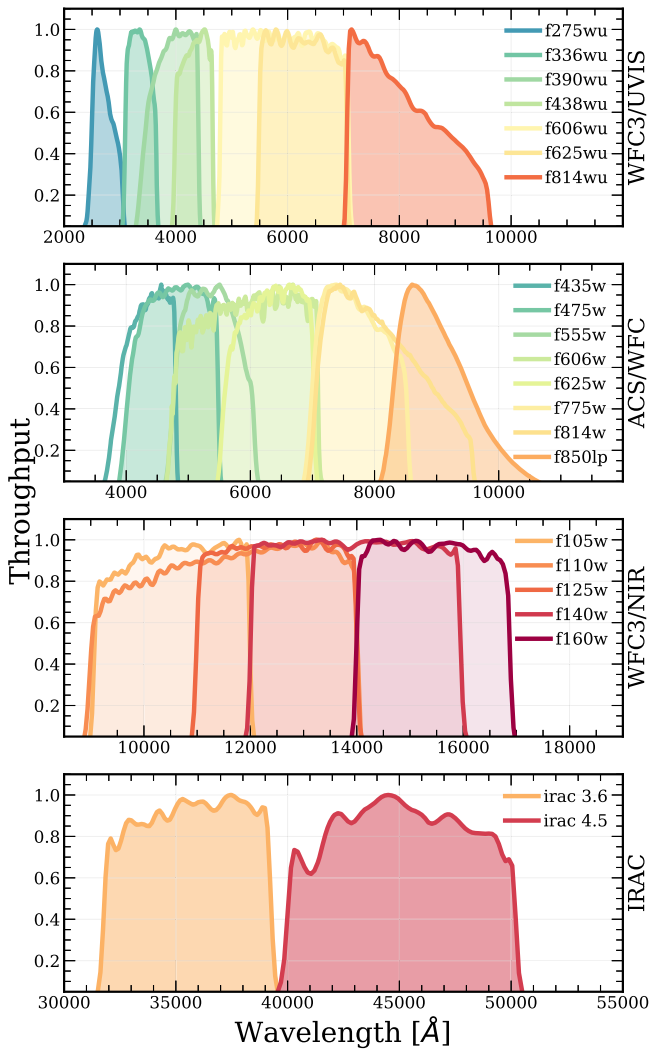


**Figure 2.** The arrangement of all available HST filters within ALCS clusters. These filters include (top to bottom): seven broad bands from WFC3/UVIS (e.g., f275wu), eight bands from ACS/WFC, five broad bands from WFC3/NIR, and two bands from Spitzer/IRAC.

this issue in our work, we use the Great Observatories Legacy Fields IR Analysis Tools, or GOLFIR, a set of tools developed to model Spitzer/IRAC and Multiband Imaging Photometer for Spitzer images based on high-resolution templates from existing HST imaging, specifically in the context of the CHARGE data.

The method follows an approach utilized in similar lensing cluster catalog works, e.g., MOPHONGO (Skelton et al. 2014; Shipley et al. 2018) and T-PHOT (Merlin et al. 2015, 2016b), and relies on using a high-resolution prior. We create this prior by combining all the available HST ACS/WFC and WFC3/IR filters to produce a weighted mosaic, based on their corresponding inverse variance maps. We then use a convolution kernel to combine the detection image with the IRAC PSF and produce the low-resolution templates. The original IRAC image is then divided into square patches, of user-defined size. These patches are also allowed to overlap, to allow for correct modeling of sources at the patch boundaries. For consistency we used a patch size of  $1/2$  with a  $0/4$  overlap for all the fields in our work. These parameters were chosen to achieve a balance between the quality of the final model image and the available computational resources.

In order to improve the quality of the extracted photometry we manually mask the brightest stars in a given field, prior to conducting the least-squares fit. We use the Gaia DR2 archive for the positions, and scale the size of the circular mask depending on the  $G$ -band magnitude of each star. We also mask all the pixels in the IRAC mosaic, for objects where the HST catalog is brighter than  $AB = 15$ . This is done to avoid large residuals in the centers of bright stars that have not been manually masked. We additionally mask all pixels where the IRAC S/N is above 80.

For the first model pass we generate IRAC model images for all objects in the HST detection catalog, brighter than  $AB = 24$ , by using the aforementioned convolved HST source cutouts, transformed into (position-dependent) IRAC PSFs. A least-squares fit of the low-resolution IRAC cutouts is then performed to the real data, where the normalization acts as the only free parameter. We additionally derive any small residual shift between the reference HST and target IRAC mosaics by using the generated IRAC model and mosaic images.

For the second model pass, we now focus on fainter HST galaxies, with  $AB < 27$ . IRAC models are then generated as before, with the least-squares normalizations now being adopted as the IRAC flux density measurement for each source. The diagonal of the covariance of the model design matrix is adopted as the photometric variance. Often there are clear systematic residuals in the fits for the brightest sources, which are likely due to a combination of (1) an imperfect transformation between the HST and IRAC PSFs, and (2) true morphological differences between F160W and the IRAC bands, for example the color gradients. To improve the IRAC morphological model for those cases, we fit the IRAC images of all sources with total S/N  $> 50$  directly with GALFIT (Peng et al. 2002) assuming a single Sérsic model (Sérsic 1963) and using the IRAC PSF. We note that we are not interested in the GALFIT parameters, but rather in the best empirical description of each IRAC morphological component. We do not adopt the “mag” of the GALFIT fit, but rather refit the model normalizations and covariances as in the previous steps, now using the GALFIT model cutouts in place of the HST-based models for the sources that have them. We show an example of the images processed with our pipeline in Figure 3, which also demonstrates the improvement in the model residuals after the GALFIT refinement.

As the IRAC flux densities are based on morphological model fits, we consider them to be on the same “total” scale as the aperture-corrected HST photometry. These are the IRAC flux densities that we will use for all our future data analysis. In addition to the model flux density fits, we also perform a simple aperture photometry measurement on our images, by using a  $D = 3''0$  apertures, similar to the approach taken in Shipley et al. (2018). Using the IRAC PSF curves of growth we then correct the aperture flux densities into total flux density. The model, aperture, and aperture-corrected flux density measurements are all available in the final version of the catalog. In Table 1 we list all the names, coordinates, and coverage areas of all 33 cluster fields covered by ALCS. We would also like to note that for the HFF, we do not make a distinction between the parallels or the cluster, and rather treat the entire mosaic, and objects within it, to be contained within a single field.

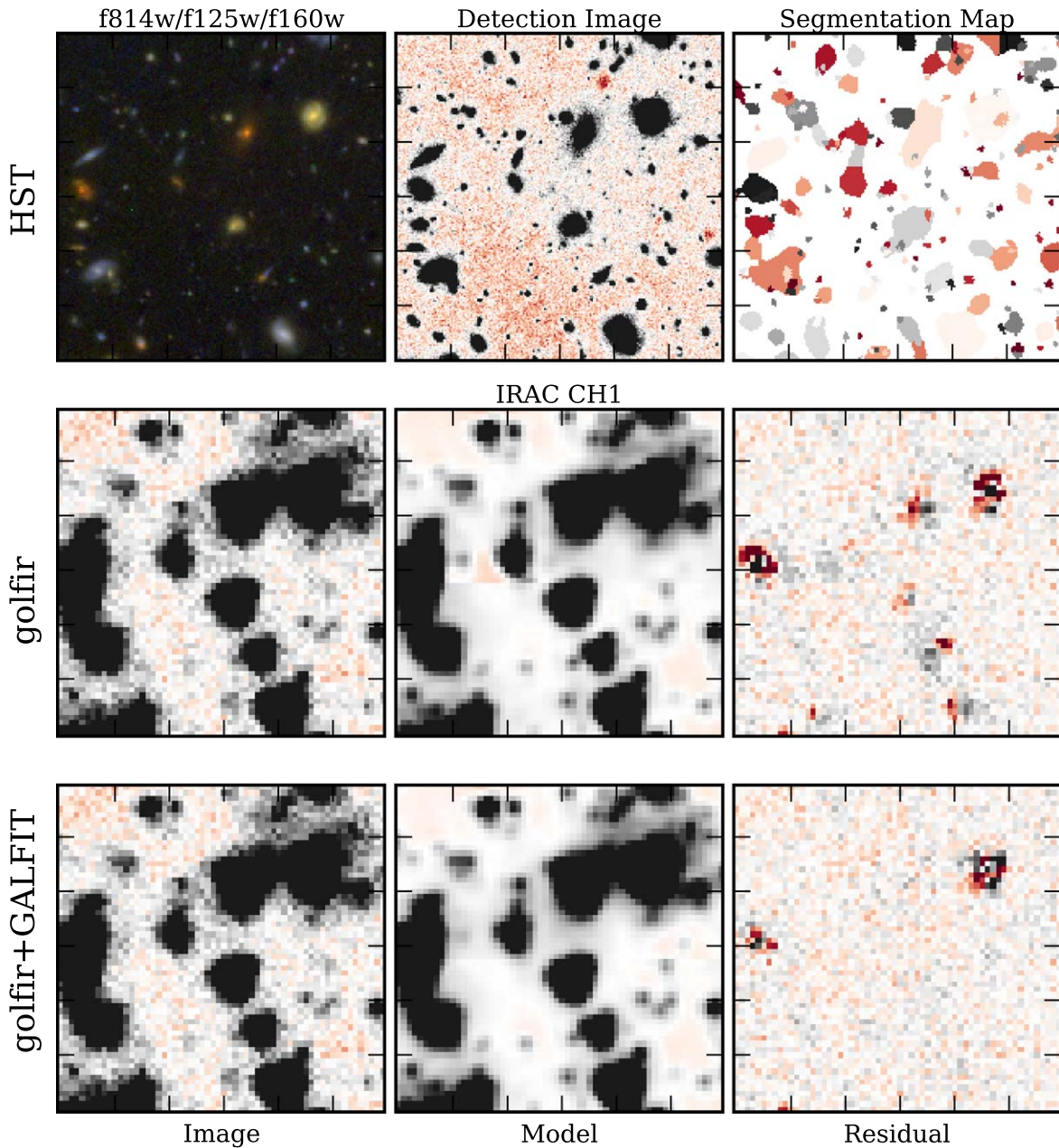


**Figure 3.** Results from the modeling procedure on the relatively crowded A370 cluster field. The cutouts are  $30''$  across, and were selected to show a wide variety of sources on the same image, i.e., the ones modeled purely with GOLFIR, and the galaxy model refined by using GALFIT. Top: The HST RGB image created from the combination of F814W, F125W, and F160W filters, the HST detection image and segmentation map. Middle: The original IRAC  $3.6\ \mu\text{m}$  science image, the GOLFIR model, and residual images. Bottom: Same as above, but now the model was additionally refined with GALFIT. The color scale has been adjusted to show the  $3\sigma$  range for each image. Most notably, the final residual mosaic can also be used to extract additional IRAC photometry for sources without an HST counterpart. The images are oriented with north up and east to the left.

## 4. Catalog

### 4.1. Atacama Large Millimeter/submillimeter Array Photometry

To further complement our photometric catalog, we have included an additional data entry containing either the measurement or the upper limit on the ALMA flux density. To do this, we start by cross-matching our objects with the ALMA continuum catalog (S. Fujimoto et al. 2022, in preparation). This catalog contains 180 sources, which have been selected with a S/N cut  $>4$ . The total flux densities are computed as a peak count, after primary beam correction in the tapered map ( $\text{mJy beam}^{-1}$ ). If no peak is identified in the

tapered map within a radius of  $1''.0$ , the pixel count at the position of the source is used instead. We do not match these sources automatically, as this approach is inadequate for nearby or highly magnified sources with complex image plane morphology. In addition to the astrometry difference, the ALMA beam size might result in erroneous counterpart assignment. Instead, we manually examine ALMA contours for each detected object, overlaid on the HST and Spitzer cutouts, and use them to assign counterparts. We feel that for crowded fields with complex lens geometry, this is the most secure approach. In Figure 4 we present a series of example stamps for three ALMA-detected objects in the SMACS0723 and A2744 fields. The rest of the 180 cutouts will be presented

**Table 1**  
Cluster Fields Covered by ALCS

Field	R.A. (deg)	Decl. (deg)	Science Area <sup>a</sup> (arcmin <sup>2</sup> )	3.6/4.5 $\mu$ m Area (arcmin <sup>2</sup> )	ALMA (1.2 mm) Area (arcmin <sup>2</sup> )	Redshift $z_{\text{spec}}$
ALCS: Hubble Frontier Fields						
AS1063	342.185	-44.530	67.8	165.1	2.3	0.348
A370	39.970	-1.577	74.4	197.9	3.3	0.375
MACSJ0416.10-2403	64.037	-24.075	68.1	191.3	2.3	0.396
A2744	3.588	-30.397	64.7	172.3	2.7	0.308
MACSJ1149.5+2223	177.401	22.399	37.6	190.5	2.6	0.543
ALCS: RELICS						
RXCJ0032.1+1808	8.046	18.130	11.6	54.0	6.4	0.396
A2537	347.093	-2.192	11.5	55.0	2.0	0.297
A3192	59.721	-29.929	11.5	55.0	4.0	0.425
MACSJ0553.4-3342	88.346	-33.708	11.5	48.2	6.9	0.430
RXC J0600.1-2007	90.041	-20.136	11.7	57.6	5.8	0.460
RXC J0949.8+1707	147.462	17.121	11.6	55.4	2.6	0.383
MACSJ0257.1-2325	44.293	-23.437	13.3	57.4	1.7	0.505
A2163	243.951	-6.127	22.0	97.7	1.5	0.203
PLCK G171.9-40.7	48.237	8.372	11.5	39.7	3.8	0.270
SMACSJ0723.3-7327	110.831	-73.454	12.2	50.7	1.6	0.390
MACSJ0035.4-2015	8.862	-20.261	12.0	58.2	2.3	0.352
MACSJ0417.5-1154	64.391	-11.906	11.7	42.1	5.0	0.443
MACSJ0159.8-0849	29.956	-8.833	11.5	57.9	2.2	0.405
ACT-CLJ0102-49151	15.750	-49.273	22.9	106.6	4.4	0.870
AbellS295	41.381	-53.040	11.8	48.5	3.2	0.300
RXC J2211.7-0350	332.941	-3.829	11.5	49.4	5.5	0.397
ALCS: CLASH						
A383	42.014	-3.529	16.8	62.0	0.8	0.187
MACS1206.2-0847	181.551	-8.801	13.1	55.0	2.0	0.440
MACS1423.8+2404	215.949	24.078	15.2	59.9	1.2	0.545
MACS1931.8-2635	292.957	-26.576	13.1	49.1	1.8	0.352
RXJ 1347-1145	206.877	-11.753	12.6	46.8	2.5	0.451
MACS1311.0-0310	197.757	-3.178	13.2	52.8	0.9	0.494
MACS1115.9+0129	168.967	1.499	13.2	53.0	1.0	0.352
MACS0429.6-0253	67.400	-2.886	13.2	54.2	0.7	0.399
RXJ2129.7+0005	322.416	0.089	18.4	75.5	0.5	0.234
MACS0329.7-0211	52.424	-2.197	12.8	48.7	2.1	0.450
MACS2129.4-0741	322.359	-7.691	14.7	55.8	1.7	0.570
A209	22.969	-13.611	15.1	54.1	0.7	0.206

**Note.**

<sup>a</sup> The ‘‘Science Area’’ corresponds to the coverage of the detection band, as defined in Section 3.

in S. Fujimoto et al. (2022, in preparation) and are also available online.<sup>35</sup> In total, we find 145/180 matches during this procedure. These are flagged with `alma_coverage = 2` in the catalog. From the 35 objects that do not have a match to our catalog, 14 are ‘‘HST dark’’ with clear detections in both IRAC channels, eight are not visible in either HST or IRAC, 10 fall outside of the HST area, but have clear IRAC detections, and three are too close to a star, or some other image artifact. The HST and IRAC ‘‘dark’’ objects are cataloged separately.

Apart from the aforementioned 145, the remaining objects in our catalog do not have reliably measured ALMA counterparts, however the ALMA continuum map at 1.2 mm still overlaps significantly with our mosaics, and as such it is still possible to extract the ALMA upper limits at the positions of our sources. We begin the extraction of upper limits by isolating a subsample of sources in our catalog that do not have an

ALMA counterpart in the continuum catalog, but still fall within an ALMA map. The objects that fall outside of ALMA coverage have been flagged with `alma_coverage = 0`. Within each field, we have used an approach similar to the original flux density extraction of S. Fujimoto et al. (2022, in preparation) and measured the flux density from the central pixel on the ALMA map. As the uncertainty on the measured flux density we adopted the noise level of the entire map (as described in S. Fujimoto et al. 2022, in preparation), calibrated to the area of the beam. This procedure results in 30,586 galaxies with a 1.2 mm upper limit, which is equivalent to  $\sim 14\%$  of the combined catalog source count of 217,958. While these are only upper limits, the addition of an extra constraint in the FIR will significantly enhance the quality of panchromatic SED fitting. For example, these measurements can help to compute the upper limits on the dust mass ( $M_{\text{dust}}$ ), for objects up to  $z \sim 7$ , and the infrared luminosity  $L_{\text{IR}}$  above  $z \sim 9$ . This is due to the fact that the 1.2 mm stops sampling the rest-frame

<sup>35</sup> [https://github.com/dawn-cph/alcs-clusters/tree/master/v1.0/alma\\_cutouts](https://github.com/dawn-cph/alcs-clusters/tree/master/v1.0/alma_cutouts)

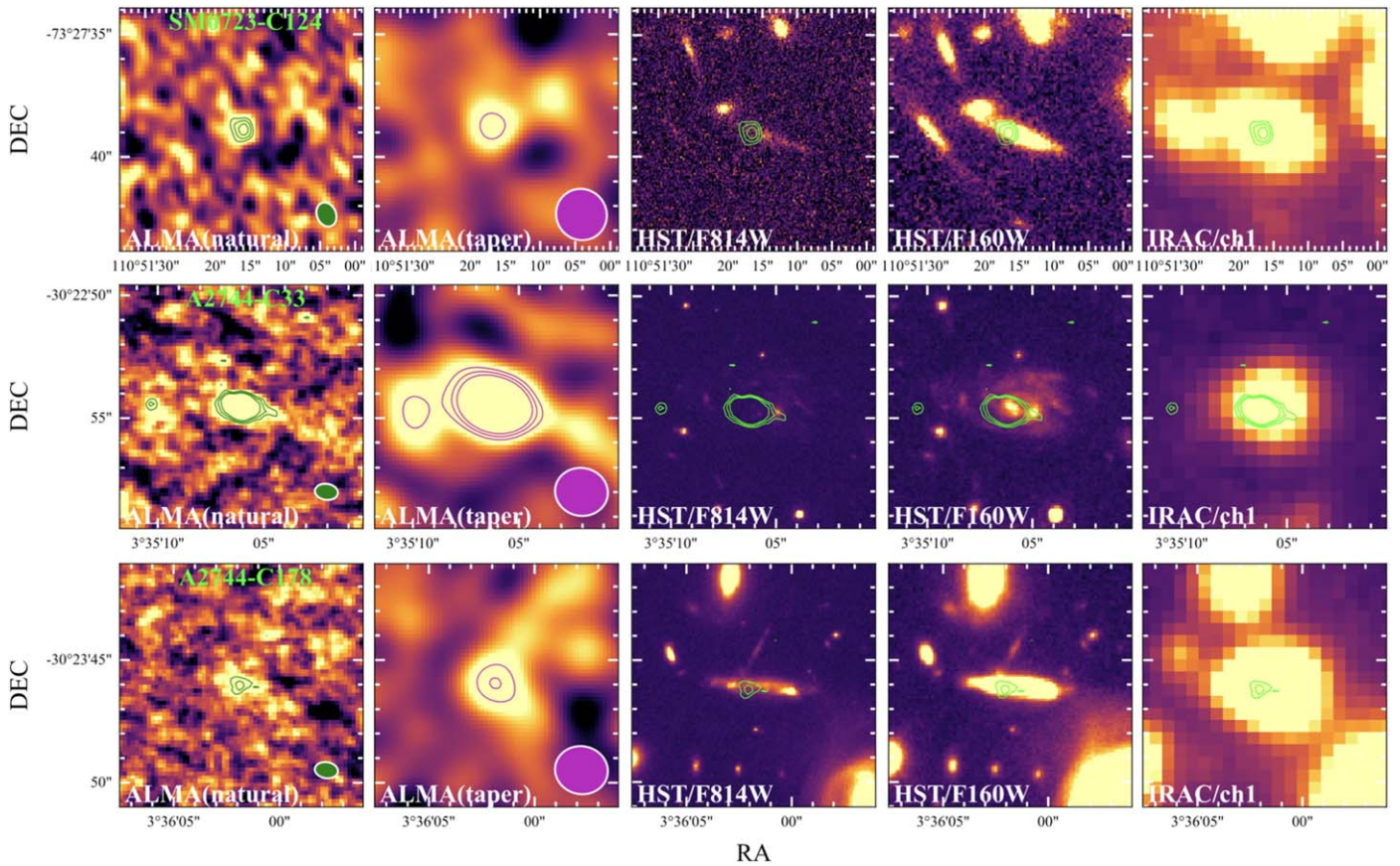


**Figure 4.** Image stamps displaying natural and tapered ALMA maps, alongside a cutout from HST/ACS, HST/WFC3, and IRAC for three sources in the SMACS0723 and A2744 fields. On top of each image we overlay 1, 2, and  $3\sigma$  contours. Green and purple shapes at the bottom of ALMA cutouts represent the size of the beam. Each panel is  $10''$  across. The remainder of the stamps for each source will be presented in an upcoming work (S. Fujimoto et al. 2022, in preparation) and are also available in the same repository as our catalogs.

continuum above  $150\ \mu\text{m}$  at  $z \sim 7$ , which is required for robust calculations of the dust mass (see, e.g., discussion in Berta et al. 2016 and Kokorev et al. 2021). In return, however, the  $80\text{--}120\ \mu\text{m}$  regime will then become available for  $1.2\ \text{mm}$  photometry at  $z = 9$ , which would allow one to sample the peak of the FIR emission and to impose tighter constraints on both total infrared luminosity,  $L_{\text{IR}}$ , and the dust temperature,  $T_{\text{dust}}$ . This naturally depends on how dusty, high- $z$  galaxies actually are, and whether the commonly used optically thin dust approximation will apply to them.

#### 4.2. Catalog Description and Flags

We provide separate multiwavelength photometric catalogs for each of the 33 clusters covered by the ALCS. Combined, the catalogs contain aperture and total flux density measurements for 218,000 sources. We list the description of the relevant columns of the catalog in Table 2. All flux densities and associated uncertainties are in units of microjansky, unless specified otherwise. For the HST data we include the aperture photometry, measured within  $D = 0''.7$ , and the associated total flux densities. The IRAC measurements are provided as the GOLFIR-modeled IRAC photometry, as well as aperture (and aperture-corrected) flux densities, measured within  $D = 3''.0$ . The cross-matched ALMA photometry is provided in units of  $\mu\text{Jy beam}^{-1}$ . We also include an ALMA source flag column, `alma_coverage`, where 2 indicates a detection, 1 an upper limit, and 0 a

**Table 2**  
Description of the Relevant Photometric Catalog Columns

Column Name	Units	Description
<code>id</code>	...	Object ID
<code>ra</code>	deg	R.A.
<code>dec</code>	deg	Decl.
<code>{filt}_flux_aper</code>	$\mu\text{Jy}$	HST $D = 0''.7$ aperture flux
<code>{filt}_err_aper</code>	$\mu\text{Jy}$	Uncertainty
<code>{filt}_flux</code>	$\mu\text{Jy}$	Total HST flux density
<code>{filt}_err</code>	$\mu\text{Jy}$	Uncertainty
<code>irac_{ch}_flux</code>	$\mu\text{Jy}$	IRAC model flux
<code>irac_{ch}_err</code>	$\mu\text{Jy}$	Uncertainty
<code>irac_{ch}_flux_aper</code>	$\mu\text{Jy}$	IRAC $D = 3''.0$ aperture flux
<code>irac_{ch}_err_aper</code>	$\mu\text{Jy}$	Uncertainty
<code>alma_coverage</code>	...	ALMA coverage flag
<code>alma_flux</code>	$\mu\text{Jy}$	ALMA flux at $1.2\ \text{mm}$
<code>alma_err</code>	$\mu\text{Jy}$	Uncertainty

lack of coverage. To help discern between the high- and low-quality photometry for sources in the catalog, we have added a number of flags which allow one to uniformly select reliable samples of objects. For each source we compute how many pixels in a  $3 \times 3$  square around the center have been masked or fall outside the IRAC mosaic. This number is given in the `n_masked` column. If the central pixel itself is masked or missing, we flag that source with `bad_phot = 1`.

**Table 3**  
Templates Used for the EAZY Fit

Parameter	Value
Optical emission: Brammer et al. (2008) <sup>a</sup>	
$A_V^b$	[0.6,0.12,0.19,0.29,1.05,2.68, 0.11,0.36,0.98,1.54,1.97,2.96]
$M/L_V$	[0.38,0.76,1.68,4.01,6.45,44.48, 0.12,0.21,0.33,0.64,1.57,4.00]
$\log_{10}(\text{sSFR})$	[-10.75, -11.37, -11.90, -12.53, -12.05, -12.47, -8.37, -8.60, -8.50, -8.57, -8.93, -8.90]

**Notes.**

<sup>a</sup> Please refer to Brammer et al. (2008) for a more detailed description of the creation and selection of these basis-set templates. See Blanton & Roweis (2007) for a methodology regarding the SFH.

<sup>b</sup> Calzetti et al. (2000).

### 4.3. Comparison to Existing Catalogs

Provided that there are existing catalogs in the lensed fields included in the ALCS, it is also useful to perform a comparison of our catalog and those presented in the literature. These include the publicly available photometric catalogs in the HFF-DeepSpace (Shingley et al. 2018), ASTRODEEP (Merlin et al. 2016a; Di Criscienzo et al. 2017), and CLASH fields (Molino et al. 2017). A series of diagnostic plots, including broadband photometry, color–color diagrams, and number counts, are fully presented and discussed in Appendix B.

## 5. Galaxy Properties

To derive the photometric redshifts, rest-frame color, dust attenuation, and stellar population parameters we have used the updated Python version of EAZY (Brammer et al. 2008). EAZY is a photometric SED fitting code which is optimized to fit nonnegative linear combinations of basis-set templates, rather than devising a solution from vast libraries of precompiled models. These templates are extracted from the Flexible Stellar Populations Synthesis (Conroy et al. 2009) models, and then reduced to a set of 12, which are able to reproduce a much larger library, spanning a variety of dust attenuation, ages, mass-to-light ratios, and star formation history (SFH) properties (see Brammer et al. 2008 and Blanton & Roweis 2007). We have listed the properties for these individual templates in Table 3. For each object in our multiwavelength catalog, EAZY integrates redshifted templates through a set of filters corresponding to our observed bands, and then finds the best combination for a given set of flux densities and associated uncertainties.

To improve the quality of the photometric redshift estimate, EAZY also implements a “template error function,” which is used to account any other miscellaneous uncertainties related to short-lived and otherwise unusual stellar populations, and the emission lines coupled to the properties of the ISM. In our analysis we have used a default template error function value of 0.2. To calculate the photometric redshifts and physical parameters with EAZY we have used total HST flux densities, calculated from the  $D = 0''.7$  aperture measurement, and the GOLFIR IRAC models. These data are contained in the “{filter}\_flux” and “irac\_{ch}\_flux” columns, respectively.

From the best-fit EAZY SEDs we derive the stellar population properties, which include, but are not limited to, the SFR,  $A_V$ ,  $M_*$ , and rest-frame colors.

### 5.1. Spectroscopic Redshift Catalogs

The ALCS fields have been covered by a wide range of spectroscopic surveys. We have examined the literature and compiled all of the available spectroscopic redshifts in order to assess the quality of our photometric redshifts. During this process we selected only the sources with robust redshift constraints, and chose the most recent source if a galaxy is present in multiple catalogs. We cross-matched all the available spectroscopic redshifts with objects in our catalog, using a  $1''.5$  matching radius. These spectroscopic redshifts are included in our main catalog, with a separate column providing the source where available.

For HFF we have used spectroscopic redshifts already compiled in Shipley et al. (2018): this includes the Grism Lens-Amplified Survey from Space (GLASS; Schmidt et al. 2014; Treu et al. 2015), and the spectral data presented in Smith et al. (2009), Owers et al. (2011), Ebeling et al. (2014), Jauzac et al. (2014), Richard et al. (2014), Balestra et al. (2016), Caminha et al. (2016), Diego et al. (2016), Grillo et al. (2016), Karman et al. (2016), Limousin et al. (2016), Lagattuta et al. (2017), and Mahler et al. (2018). Where appropriate, we also have updated the spectroscopic redshifts with the most recent results from Richard et al. (2021). In total we recover 5055 matches with our catalog, in all five HFF fields, including the parallels. Please note, however, that the number of spectroscopic redshifts in the parallel fields is severely limited. We include them in our final comparison for the record.

For CLASH we have compiled the most recent data from GLASS (Schmidt et al. 2014; Treu et al. 2015), and the results from Caminha et al. (2019) and Richard et al. (2021). In total there are 2090 matches with our catalog, spanning 10 out of 12 CLASH fields. Finally, for the RELICS spectroscopic redshifts, we have used the data from Richard et al. (2021) for RXC0600, and a compilation of spec- $z$  data presented in A. Guerrero et al. (2022, in preparation). In total we find 351 matches with our catalogs. The full list of fields and matches is outlined in Table 4.

### 5.2. Photometric Redshift Accuracy

To quantify the precision of our photo- $z$  estimate we used the normalized median absolute deviation (NMAD; Hoaglin et al. 1983), defined as

$$\sigma_{\text{NMAD}} = 1.48 \times \text{median} \left( \frac{|\Delta z - \text{median}(\Delta z)|}{1 + z_{\text{spec}}} \right). \quad (1)$$

This method is commonly used in the literature (see, e.g., Skelton et al. 2014; Shipley et al. 2018), allowing for a quick and unbiased comparison of redshift quality between different catalogs, and is also less sensitive to outliers, as described in Brammer et al. (2008). The outlier fraction  $\eta$  is given by  $|\Delta z|/(1+z_{\text{spec}}) > 0.15$ , following the methodology described in Hildebrandt et al. (2012).

In total we have carried out the comparison for 7107 matched objects, excluding catastrophic outliers, spanning 24 fields, as shown in Figure 5. We find that our redshift accuracy

**Table 4**  
Sources of Spectroscopic Redshift

Field	Matches (No. of Galaxies)
HFF: Cluster and Parallel	
A2744	736
A370	793
MACSJ0416	1852
MACSJ1149	1173
AS1063	501
CLASH	
MACS0329	129
MACS0429	129
MACS1115	66
MACS1206	424
MACS1311	68
RXJ_1347	511
MACS1423	154
MACS1931	138
MACS2129	322
RXJ2129	149
RELICS	
RXC J0600	73
ACT-CLJ0102-49151	76
AbellS295	15
A2163	44
A2537	37
MACSJ0159.8-0849	9
MACSJ0257.1-2325	11
MACSJ0417.5-1154	25
MACSJ0553.4-3342	61

is generally good, with a  $\sigma_{\text{NMAD}}$  of 0.0406, and 20.6% of catastrophic failures.

For both the  $z_{\text{phot}} - z_{\text{phot}}$  and  $z_{\text{phot}} - z_{\text{spec}}$  comparisons, we note the existence of overdensities located either at  $z \sim 1$  or  $z \sim 4$ , for which  $\Delta z \sim 3$ . This is where a vast majority of our catastrophic outliers are located. These redshift discrepancies are caused by the misidentification between the Lyman (912 Å) and the Balmer (3644 Å) breaks, as well as the 4000 Å break, in the fitted SEDs. The manifestation of the break confusion is a consequence of degenerate behavior of templates, when faced with either sparse or very faint photometry, and is particularly prominent when we compare large samples of photometric redshifts between different catalogs.

### 5.3. Gravitational Lensing Magnification

For objects within the cluster fields we compute and provide the lensing magnification factor ( $\mu$ ), which is based on the R.A., decl. coordinate of the source in the detection band (i.e., the peak flux density coordinate) and its redshift. Although a vast majority of sources in a given field only have a  $z_{\text{phot}}$  estimate, we use a  $z_{\text{spec}}$  where possible. Following the methodology described in Sun et al. (2022), we use the Zitrin-NFW lens models (Zitrin et al. 2013, 2015) for the HFF and CLASH clusters, and GLAFIC models (Oguri 2010; Okabe et al. 2020) for RELICS. These models consist of the mass surface density ( $\kappa$ ) and weak lensing shear ( $\gamma$ ) maps. We

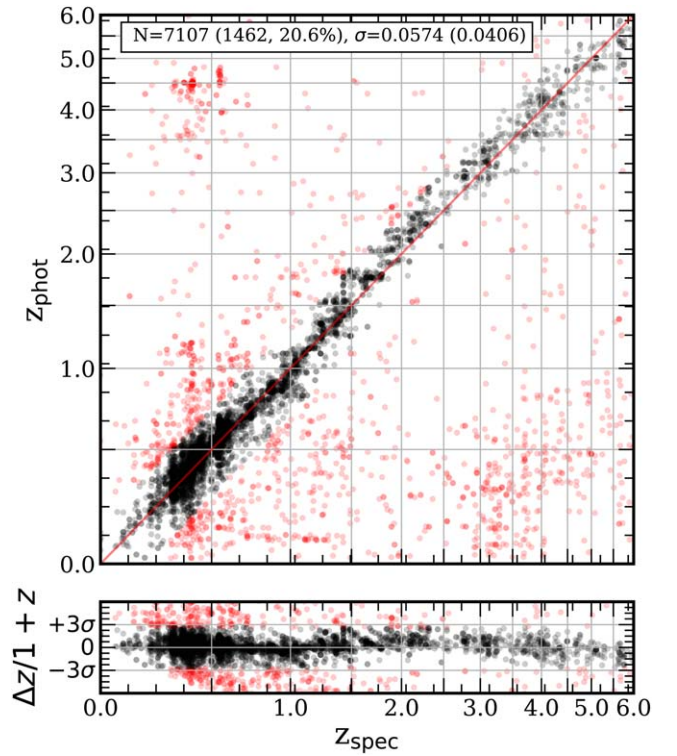


**Figure 5.** Comparison between photometric redshifts derived by EAZY and the spectroscopic redshift from the literature. We have carried out the comparison in all fields where a match was found; in total, these include all five Frontier Fields, 10 CLASH fields, and nine RELICS field. Black and red circles denote galaxies below and above the catastrophic limit of 0.15, respectively.

then compute the magnification by using

$$\mu = \frac{1}{(1 - \kappa \beta)^2 - (\gamma \beta)^2}, \quad (2)$$

where  $\beta$  is the lensing depth, defined as  $\beta = D_{\text{ls}}/D_s$ , with  $D_{\text{ls}}$  being the angular diameter distance between the lens and the source, and  $D_s$  is the angular diameter distance to the source. Similarly to Rawle et al. (2016), if the source redshift  $z_s$  is below or within the cluster redshift  $z_{\text{cl}}$ , namely  $z_s \leq z_{\text{cl}} + 0.1$ , we set the magnification to unity. Sources that fall outside of the magnification maps for a given field are not expected to be significantly affected by gravitational lensing. For these, we have set  $\mu = 1$ . In Figure 6 we present the distributions of best-fit photometric redshifts and magnification values for all objects in our catalog. Please note that we do not apply these lensing corrections to any flux densities listed in our catalog.

We present the distribution of the demagnified  $M_*$  with redshift in Figure 7. In addition to that, we also highlight the ALMA-detected ALCS sources, including the Fujimoto et al. (2021) object at  $z = 6.07$ . We note that ALMA-detected objects are more massive when compared to the other galaxies in the catalog. A similar trend has been observed in both the  $M_{1500}$  versus  $z$  and  $M^*$  versus  $z$  relations in Dunlop et al. (2017).

### 5.4. Red Sequence

In lieu of secure spectroscopic redshifts, a definitive assessment of cluster membership for galaxies in our catalog cannot be achieved. While the  $z_{\text{phot}}$  probability density functions,  $p(z)$ , and the comparison to  $z_{\text{spec}}$  via  $\sigma_{\text{NMAD}}$  can

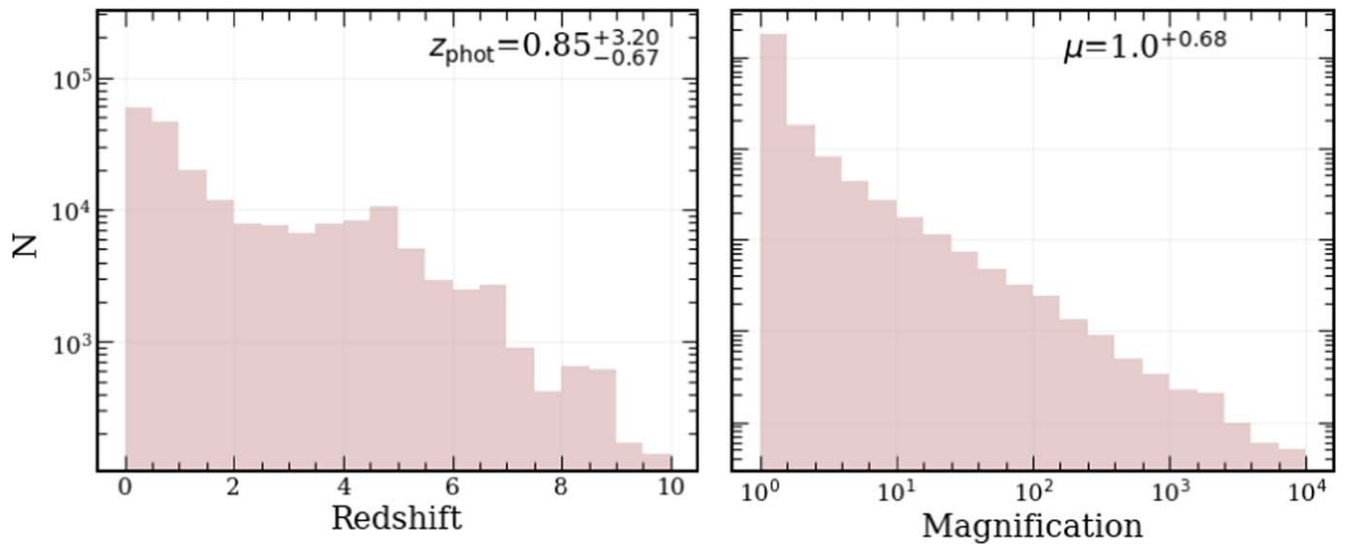


**Figure 6.** The log-scaled distribution of best-fit photometric redshifts (left) and computed magnification factors (right) for the full catalog. The median and the 68% confidence interval for each parameter are shown on each plot.

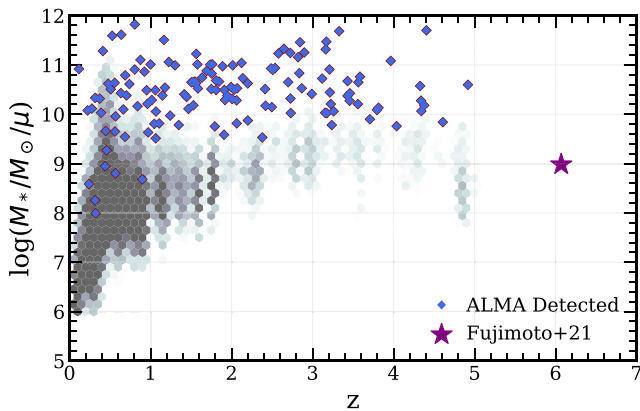


**Figure 7.** A density plot of EAZY-derived demagnified stellar mass as a function of redshift. ALMA-detected galaxies are shown as blue diamonds. A bright, multiply lensed  $z = 6.07$  source from Fujimoto et al. (2021) is shown as a purple star.

provide us with important hints regarding the robustness of photometric redshifts, an additional quality test is required.

We can exploit the observational fact which dictates that the majority of early-type galaxies (ETGs), that consist in massive clusters display a tight color–magnitude correlation. This relation has been referred to as the Cluster Red Sequence, or just the red sequence (Gladders & Yee 2000). This color–magnitude relation was shown to hold from cluster to cluster (López-Cruz et al. 2004) and also displays a relatively small scatter (Bower et al. 1992). The technique provides an independent redshift constraint for galaxies contained within clusters, with the ETG overdensities being exploited as a cluster marker for quite some time in the literature (López-Cruz 1997; Gladders et al. 1998; Kaiser et al. 1998; Yee et al. 1999; Lubin et al. 2000; López-Cruz et al. 2004).

Effectively, the cluster galaxies which should lie on the red sequence can be isolated from the field objects with only two filters that cover the 4000 Å break. For our data set this can be achieved through a combination of the F435W and F606W HST/ACS filters. In Figure 8 we present a red-sequence diagnostic plot for the HFF galaxies that are considered to be within clusters based on their photometric redshift

( $|z_{\text{phot}} - z_{\text{cluster}}| \leq 0.1$ ) and that are also bright ( $m_{\text{F606W}} < 25$ ). By examining the distribution of galaxies as a function of redshift we note the presence of distinct density peaks located in proximity to the cluster redshift. The color–magnitude diagnostic plot also reveals that the galaxies which we have selected to be a part of the cluster based on the  $z_{\text{phot}}$  tend to form a distinct color sequence on the diagnostic plot. From the combination of both  $\sigma_{\text{NMAD}}$  and red-sequence diagnostics, we conclude that the recovered photometric redshifts, and the stellar population parameters derived based on them, are robust both for the field and cluster galaxies in our catalogs.

### 5.5. Rest-frame Color Galaxy Classification

Comparison of galaxies at different redshifts often requires rest-frame, rather than observed frame, colors to be used. For each galaxy these are determined by assuming the best-fit EAZY template and its redshift, in order to calculate the rest-frame flux density for a set of filters. The rest-frame colors are then computed by integrating a transmission curve for a given filter through the best-fit template, as described in Brammer et al. (2011). In our final catalogs we provide the rest-frame flux densities for the most commonly used filters (GALEX *NUV*, COSMOS *r*, Johnson *U*, *B*, *V*, and *J*).

The rest-frame flux densities can be used to assess the galaxy populations in each field by using color–color analysis. Multiple previous studies have devised a variety of techniques to classify galaxies based on broadband photometry. One such prescription utilizes the  $U - V$  and  $V - J$  rest-frame colors (Labbé et al. 2005; Wuyts et al. 2007; Williams et al. 2009) to separate galaxies into quiescent and star-forming categories. Quiescent galaxies with low levels of star formation are red in the  $U - V$  regime and are easily distinguished from the similarly red (in  $U - V$ ), dusty, star-forming galaxies, with the  $V - J$  color. An alternative method, using the  $NUV - r - J$  colors, instead, has been proposed by Ilbert et al. (2013) and Arnouts et al. (2013). While the  $UVJ$  selection is the most commonly used approach in the literature, the  $NUVrJ$  method has some key advantages. The shorter-wavelength *NUV* band is more sensitive both to the dust attenuation and emission from young stellar populations than the *U* band. Although the

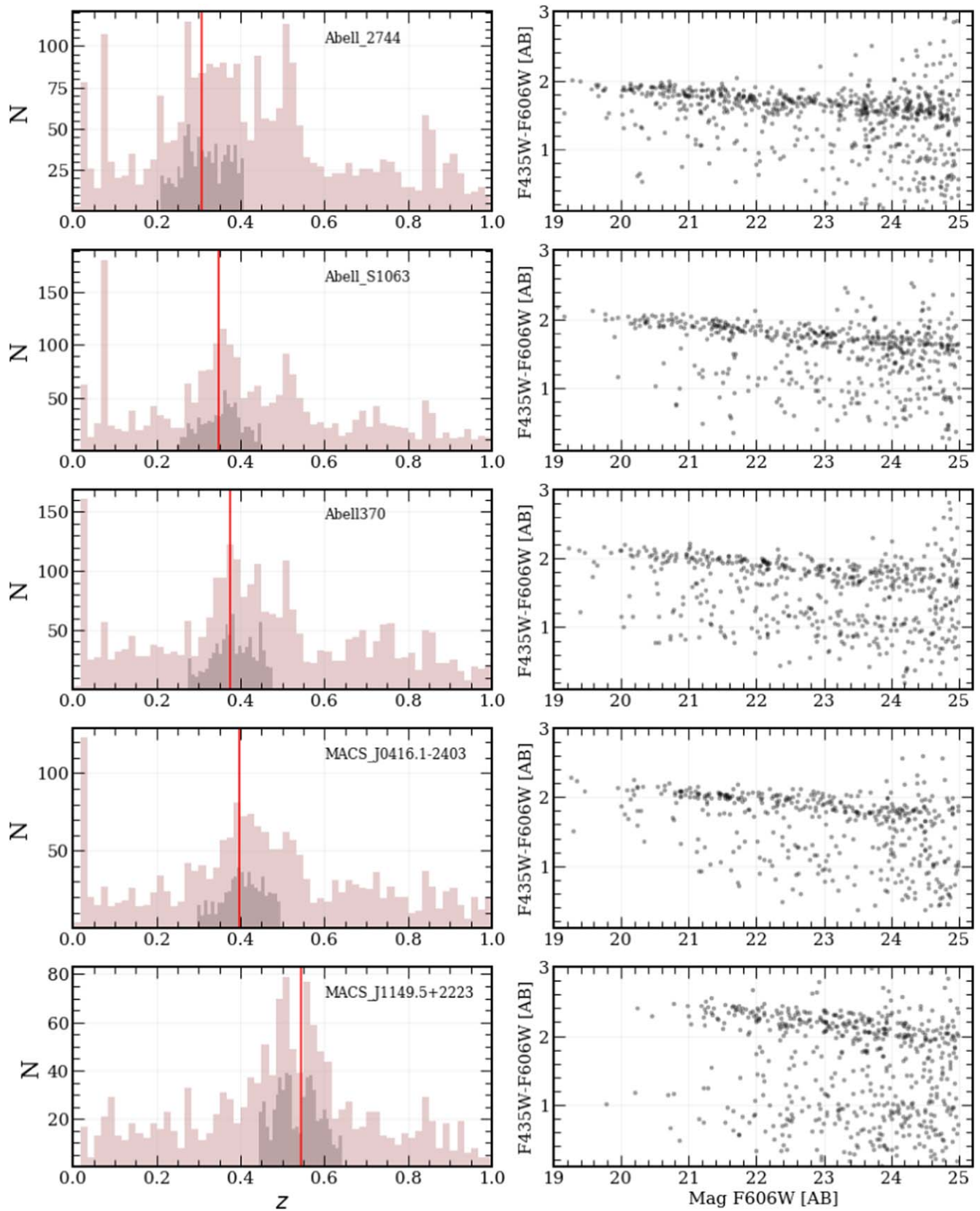


**Figure 8.** Red-sequence diagnostic for galaxies within the Hubble Frontier Fields. Left: A histogram of all objects in the catalog in the  $0 < z < 1$  range (red) and an isolated sample of galaxies which we consider to belong to the cluster (gray),  $|z - z_{\text{cl}}| < 0.1$ , and  $F606W < 25$  AB mag. The vertical red line represents the redshift of the cluster. Right: color–magnitude diagnostics of the red sequence with the F435W and F606W filters.

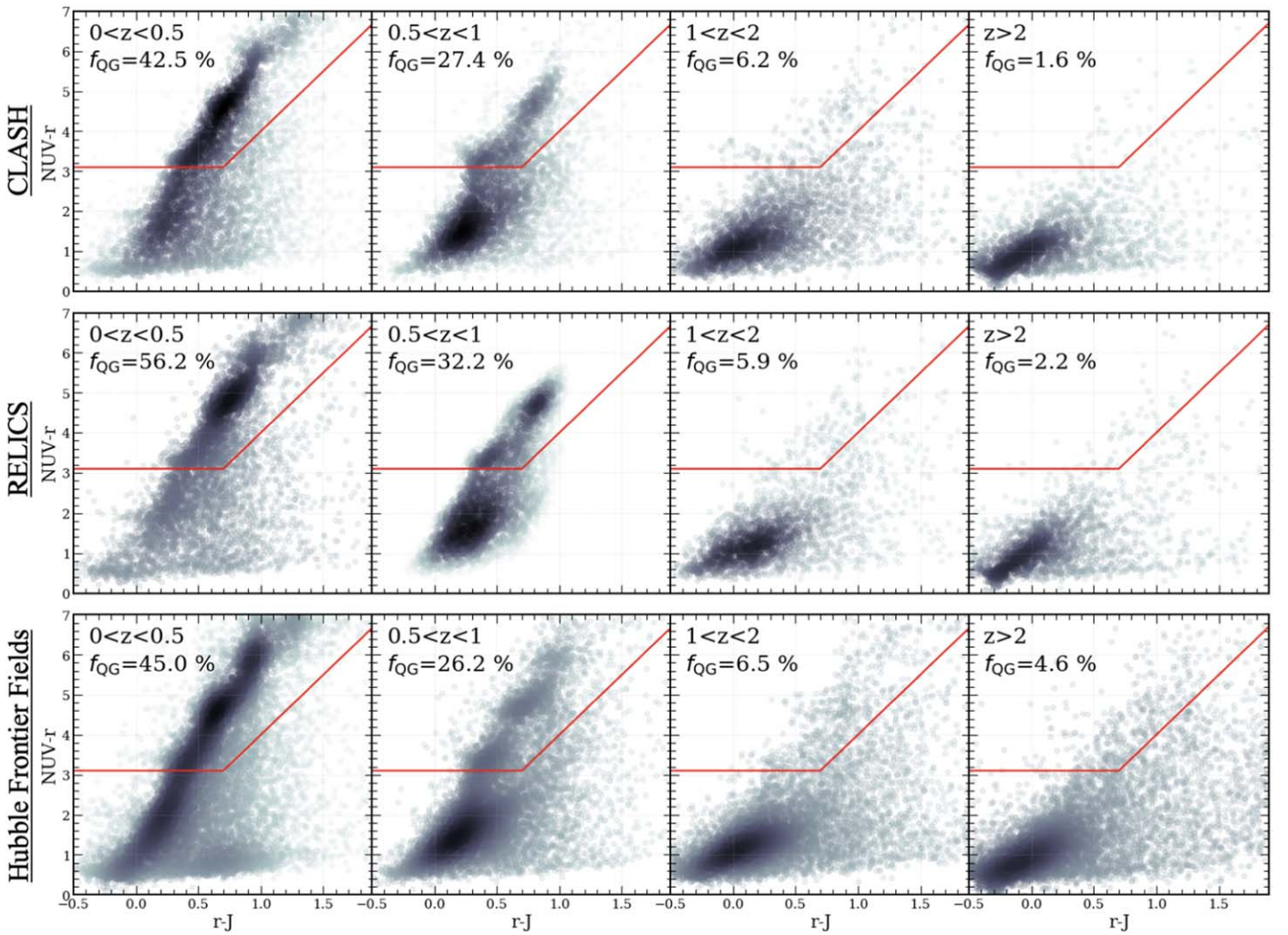


**Figure 9.** Classification of galaxies for all ALCS fields by using the  $NUV - r$  and  $r - J$  rest-frame colors. The  $NUV - r - J$  galaxy selection prescription from Ilbert et al. (2013) is shown as a solid red line. The fraction of quiescent galaxies (QGs) is displayed within each plot. Here we have limited our selection to only include galaxies with  $nusefilt \geq 5$  and a  $S/N > 5$  in the HST f160w filter.

amount of quiescent galaxies at  $z > 2$  is limited (see, e.g., Ilbert et al. 2013; Muzzin et al. 2013; Davidzon et al. 2017), the rest-frame  $NUV$  will still be covered by the optical photometry at that redshift regime, which is no longer the case for the rest-frame  $U$  band. This, in return, would make the  $NUVrJ$  selection technique more reliable at higher redshifts. In our paper we adopt the  $NUVrJ$  selection, however the  $U$  and  $V$  rest-frame flux densities are also provided in our final catalog. We display our selection in Figure 9, where the quiescent galaxies tend to be located in the upper-left corner of the diagram, with the boundaries defined in Ilbert et al. (2013):

$$NUV - r = \begin{cases} 3(r - J) + 1 & \text{for } r - J > 0.7 \\ 3.1 & \text{for } r - J < 0.7. \end{cases}$$

When comparing the  $UVJ$  and  $NUVrJ$  color-classification methods,  $\sim 70\%$  of objects selected with  $NUVrJ$  overlap with  $UVJ$  quiescent candidates, varying slightly with the depth of our field of choice, and therefore its redshift distribution. Overall we find that 17% of objects in HFF, 23% in RLC, and 17% in CLS are located in the upper quadrant of the  $NUVrJ$  diagram, and can thus be classified as quiescent. The ALCS covers cluster fields, where the star formation is generally expected to be suppressed, especially at low redshift (see, e.g.,

Boselli et al. 2016, and references therein). Therefore it is not at all surprising for us to recover high fractions of quiescent galaxies.

## 6. Conclusions

This paper describes the creation of a HST+IRAC photometric and galaxy property catalog within the 33 lensed cluster fields covered by the 134 arcmin<sup>2</sup> ALCS survey. The mosaics and catalogs cover a combined area of  $\sim 690$  arcmin<sup>2</sup>, in 33 ALCS fields, which include five HFF, 16 RELICS, and 12 CLASH fields. The final catalog numbers roughly 218,000 sources, which are covered by, at most, 12 HST/ACS, UVIS, and WFC3 bands, plus the additional IRAC photometry at 3.6 and 4.5  $\mu\text{m}$ . To process these data we have reprocessed and recombined all the available archival HST exposures, now combined into a single CHARGE data set, as well as all available IRAC data covering the same fields. Each image has been aligned to the same highly precise Gaia DR2 reference frame, ensuring a robust internal alignment of the HST and IRAC images for matched-aperture photometry, with the final absolute astrometric precision generally being  $< 100$  mas.

In our analysis, we have applied a consistent methodology in order to compute multiwavelength photometry across all 33

fields. The SEP software (Barbary 2016) is used to detect sources on a weighted master detection image from all available ACS/WFC and WFC3/IR filters of a given field. We do not PSF match the HST images; instead, we extract the photometry for each filter separately, with apertures of varying sizes, and then correct it to total flux densities by using curves of growth. We use a novel GOLFIR algorithm, which relies on using the IRAC PSF-convolved high-resolution mosaics as a prior, to model and extract the IRAC photometry. Furthermore, we test the robustness of our derived photometry by comparing it to the publicly available HFF-DeepSpace (Shipley et al. 2018) and ASTRODEEP (Merlin et al. 2016a; Di Criscienzo et al. 2017) catalogs in the HFF, and the photometric CLASH catalog of Molino et al. (2017). In all cases we find results which are consistent, despite using a different approach. Moreover, compared to the aforementioned catalogs, the CHARGE data covers a  $\sim \times 2$  area, and thus presents a substantial improvement in terms of the number of objects available.

To derive photometric redshifts and stellar population parameters, we use the SED fitting software EAZY (Brammer et al. 2008). For the fields where uniform spectroscopic data is available (24/33), we achieve an average NMAD of 0.0406, for the photometric and spectroscopic redshifts across all fields, with an outlier fraction of 21%. To accompany our photometric redshifts, we provide stellar masses, SFRs, extinctions, and other stellar population parameters based on the observed photometry. We also compute and use the rest-frame  $NUVrJ$  colors to separate our galaxies into potentially star-forming and quiescent samples. We find that our lensed cluster sample data contains an increased fraction of quiescent galaxies compared to that of blind field observations. In addition to that, we use all the available magnification maps in the ALCS fields, and provide with our catalog magnification factors, where possible. We manually cross-match our data with the 145  $S/N > 4$  ALMA-detected galaxies, and provide upper limit measurement for a further  $\sim 30,000$  sources.

These mosaics and catalogs, produced by the ALCS team, conclude one of the initial phases of the entire project, which, as outlined in Section 2, will focus on multiple aspects and properties of faint submillimeter sources. These catalogs will also facilitate the detection and further examination of the optically dark galaxy populations (e.g., Wang et al. 2019; Sun et al. 2021; Shu et al. 2022). As such, these photometric catalogs can act as an important tool in designing future observations (e.g., with Keck/MOSFIRE, JWST, Giant Magellan Telescope) in an attempt to elucidate the key questions about the early onset of star formation, reionization, and assembly of the first galaxies.

Both the HST/Spitzer mosaics and photometric catalogs described in this work are publicly available in FITS format, through our repository.<sup>36</sup> Alongside the photometric catalogs for each ALCS field, we include mosaics for all filters, detection images, segmentation maps, bright star masks, IRAC models, and residuals. We also provide photometric redshifts and stellar population properties, as measured by EAZY, for each field. In the repository we also provide all the technical documentation regarding the source detection and modeling parameters, as well as notebooks to reproduce best-fit EAZY SEDs.

We thank the anonymous referee for a number of constructive suggestions, which helped to improve this manuscript. We thank Ian Smail for his helpful suggestions. The Cosmic Dawn Center is funded by the Danish National Research Foundation under grant No. 140. G.E.M. acknowledges the Villum Fonden research grant 13160 “Gas to stars, stars to dust: tracing star formation across cosmic time,” grant 37440, “The Hidden Cosmos,” and the Cosmic Dawn Center of Excellence funded by the Danish National Research Foundation under the grant No. 140. F.V. acknowledges support from the Carlsberg Foundation research grant CF18-0388 “Galaxies: Rise And Death”. I.D. acknowledges support from the European Union’s Horizon 2020 research and innovation program under the Marie Skłodowska-Curie grant agreement No. 896225. S.T. and G.B. acknowledge support from the European Research Council (ERC) Consolidator Grant funding scheme (project ConTExt, grant No. 648179). K.K. acknowledges the support by JSPS KAKENHI grant No. JP17H06130 and the NAOJ ALMA Scientific Research grant No. 2017-06B. F.S. acknowledges support from the NRAO Student Observing Support (SOS) award SOSPA7-022. D.E. acknowledges support from the Beatriz Galindo senior fellowship (BG20/00224) from the Spanish Ministry of Science and Innovation, projects PID2020-114414GB-I00 and PID2020-113689GB-I00 financed by MCIN/AEI/10.13039/501100011033, project P20\_00334 financed by the Junta de Andalucía, and project A-FQM-510-UGR20 of the FEDER/Junta de Andalucía-Consejería de Transformación Económica, Industria, Conocimiento y Universidades. This work is based on observations taken by the RELICS Treasury Program (GO 14096) with the NASA/ESA HST, which is operated by the Association of Universities for Research in Astronomy, Inc., under NASA contract NAS5-26555.

*Facilities:* HST, Spitzer/IRAC, ALMA.

*Software:* Astrodrizzle (Hack et al. 2012), EAZY (Brammer et al. 2008), FSPS (Conroy et al. 2009), GALFIT (Peng et al. 2002, 2010), grizli (Brammer & Matharu 2021), golfir (Brammer 2022), MOPHONGO (Labbé et al. 2013, 2015), sep (Barbary 2016), SExtractor (Bertin & Arnouts 1996).

## Appendix A Data Description

Both the mosaics and photometric catalogs described in this work are publicly available in FITS format via our repository (<https://github.com/dawn-cph/alcs-clusters/>). The data are also available under a Creative Commons Attribution license via the Electronic Research Data Archive (ERDA) at the University of Copenhagen at doi:10.17894/ucph.aefebd02-b683-4ae8-8731-5b4c7808a7ec.

For each field we make available the science, `sci`, and inverse variance, `wht`, mosaics for each HST filter. The units of the filter mosaics are electrons  $s^{-1}$ , with the photometric calibration to cgs units provided in the `PHOTFLAM` ( $f_\lambda$ ) and `PHOTFNU` ( $f_\nu$ ) header keywords. For IRAC 3.6  $\mu m$  and 4.5  $\mu m$  we also provide the science `sci` and inverse variance `wht` maps. In addition to that we include the model and the residual images for the GOLFIR fit are included in the `model` files. The units for all IRAC images are given in microjansky.

A listing of detection parameters from SEP is shown in Table 5. Each photometric catalog includes the source id, position, aperture and total photometry in all available filters, as well as photometric redshifts and physical parameters as

<sup>36</sup> <https://github.com/dawn-cph/alcs-clusters>

**Table 5**  
SEP Parameters Used for HST Source Detection and Aperture Photometry

Parameter	Value
BACK_FILTERSIZE	4''0
BACK_FILTER	3
FILTER	Y
FILTER_NAME	F160W
CLEAN	Y
DEBLEND_CONT	0.001
DEBLEND_NTHRESH	32
MINAREA	9
THRESHOLD	1.0

**Table 6**  
Encircled Energy Correction for  $D = 0.''7$  Apertures

Filter	Encircled Energy Fraction
WFC3/NIR	
F105W	0.839
F110W	0.830
F125W	0.825
F140W	0.815
F160W	0.803
ACS/WFC	
F435W	0.887
F475W	0.893
F555W	0.895
F606W	0.896
F625W	0.896
F775W	0.894
F814W	0.889
F850LP	0.853
WFC3/UVIS	
F275WU	0.856
F336WU	0.881
F390WU	0.891
F438WU	0.897
F606WU	0.899
F625WU	0.898
F814WU	0.890

**Table 7**  
Effective Depths of HST/Spitzer Data

Field	HST/f814w	HST/f125w	HST/f160w Median $1\sigma$ depth <sup>a</sup> ( $\mu$ Jy)	IRAC 3.6 $\mu$ m	IRAC 4.5 $\mu$ m
ALCS: Hubble Frontier Fields					
AS1063	0.0097	0.0186	0.0210	0.0437	0.0332
A370	0.0075	0.0221	0.0270	0.0467	0.0408
MACSJ0416.10-2403	0.0060	0.0183	0.0237	0.0417	0.0307
A2744	0.0087	0.0201	0.0256	0.051	0.0392
MACSJ1149.5+2223	0.0037	0.0053	0.0078	0.0432	0.0358
ALCS: RELICS					
RXCJ0032.1+1808	0.0210	0.0455	0.0292	0.1621	0.1390
A2537	0.0240	0.0496	0.0336	0.1725	0.1472
A3192	0.0129	0.0469	0.0277	0.1501	0.1093
MACSJ0553.4-3342	0.0127	0.0439	0.0252	0.0963	0.0690
RXC J0600.1-2007	0.0190	0.0477	0.0288	0.1581	0.1253

**Table 7**  
(Continued)

Field	HST/f814w	HST/f125w	HST/f160w Median $1\sigma$ depth <sup>a</sup> ( $\mu$ Jy)	IRAC 3.6 $\mu$ m	IRAC 4.5 $\mu$ m
RXC J0949.8+1707	0.0231	0.0576	0.0372	0.1631	0.1324
MACSJ0257.1-2325	0.0107	0.0462	0.0287	0.1760	0.1628
A2163	0.0166	0.0496	0.0465	0.1265	0.1461
PLCK G171.9-40.7	0.0263	0.0531	0.0351	0.1526	0.1354
SMACSJ0723.3-7327	0.0219	0.0150	0.0173	0.0638	0.0483
MACSJ0035.4-2015	0.0238	0.0397	0.0251	0.1634	0.1292
MACSJ0417.5-1154	0.0228	0.0448	0.0371	0.1689	0.1263
MACSJ0159.8-0849	0.0218	0.0411	0.0257	0.1646	0.1405
ACT-CLJ0102-49151	0.0189	0.0400	0.0234	0.0688	0.0533
AbellS295	0.0160	0.0426	0.0250	0.0839	0.0631
RXC J2211.7-0350	0.0237	0.0527	0.0340	0.1495	0.1258
ALCS: CLASH					
A383	0.0147	0.0211	0.0211	0.1278	0.1647
MACS1206.2-0847	0.0154	0.0203	0.0225	0.1872	0.1495
MACS1423.8+2404	0.0107	0.0132	0.0144	0.0632	0.0516
MACS1931.8-2635	0.0195	0.0221	0.0220	1.2199	0.1568
RXJ 1347-1145	0.0115	0.0201	0.0152	0.0529	0.0482
MACS1311.0-0310	0.0161	0.0201	0.0211	0.1874	0.1609
MACS1115.9+0129	0.0165	0.0204	0.0214	0.1024	0.0629
MACS0429.6-0253	0.0147	0.0181	0.0206	0.1786	0.1496
RXJ2129.7+0005	0.0151	0.0170	0.0174	0.1608	0.1299
MACS0329.7-0211	0.0150	0.0183	0.0191	0.1790	0.1493
MACS2129.4-0741	0.0113	0.0231	0.0209	0.0616	0.0533
A209	0.0154	0.0203	0.0183	0.1223	0.1384

**Note.**<sup>a</sup> Computed directly from the final photometric catalogs.**Table 8**  
HST Image Sources

Field	Filters	Instrument	Proposal ID	Proposal PI
ALCS: Hubble Frontier Fields				
AS1063	F435W, F475W, F606W, F625W	ACS/WFC	12458	Postman, Marc
	F775W, F814W, F850LP	ACS/WFC	12458	Postman, Marc
	F814W	ACS/WFC	13063	Riess, Adam
	F814W	ACS/WFC	13459	Treu, Tommaso L.
	F435W, F606W, F814W	ACS/WFC	14037	Lotz, Jennifer
	F435W, F606W	ACS/WFC	14209	Siana, Brian
	F606W, F814W	ACS/WFC	15117	Steinhardt, Charles L.
	F606W, F814W	ACS/WFC	15936	Kelly, Patrick
	F475W	ACS/WFC	15940	Ribeiro, Bruno
	F606W, F814W	ACS/WFC	16278	Kelly, Patrick
	F105W, F110W, F125W, F140W, F160W	WFC3/IR	12458	Postman, Marc
	F125W, F160W	WFC3/IR	13063	Riess, Adam
	F105W, F140W	WFC3/IR	13459	Treu, Tommaso L.
	F105W, F125W, F140W, F160W	WFC3/IR	14037	Lotz, Jennifer
	F105W, F125W, F160W	WFC3/IR	15117	Steinhardt, Charles L.
	F110W	WFC3/IR	16729	Kelly, Patrick
	F225W, F275W, F336W, F390W	WFC3/UVIS	12458	Postman, Marc
	F275W, F336W	WFC3/UVIS	14209	Siana, Brian
	F225W	WFC3/UVIS	15940	Ribeiro, Bruno
	F225W, F275W	WFC3/UVIS	16239	Foley, Ryan
F606W	WFC3/UVIS	16729	Kelly, Patrick	
A370	F475W, F625W, F814W	ACS/WFC	11507	Noll, Keith S.
	F475W	ACS/WFC	11582	Blain, Andrew
	F814W	ACS/WFC	11591	Kneib, Jean-Paul Richard
	F814W	ACS/WFC	13459	Treu, Tommaso L.

**Table 8**  
(Continued)

Field	Filters	Instrument	Proposal ID	Proposal PI
ALCS: Hubble Frontier Fields				
	F814W	ACS/WFC	13790	Rodney, Steve
	F435W, F606W, F814W	ACS/WFC	14038	Lotz, Jennifer
	F435W, F606W	ACS/WFC	14209	Siana, Brian
	F606W, F814W	ACS/WFC	15117	Steinhardt, Charles L.
	F475W	ACS/WFC	15940	Ribeiro, Bruno
	F606W, F814W	ACS/WFC	16278	Kelly, Patrick
	F140W	WFC3/IR	11108	Hu, Esther M.
	F110W, F160W	WFC3/IR	11591	Kneib, Jean-Paul Richard
	F160W	WFC3/IR	12880	Riess, Adam
	F105W, F140W	WFC3/IR	13459	Treu, Tommaso L.
	F110W, F125W, F160W	WFC3/IR	13790	Rodney, Steve
	F105W, F125W, F140W, F160W	WFC3/IR	14038	Lotz, Jennifer
	F160W	WFC3/IR	14216	Kirshner, Robert P.
	F105W, F125W, F160W	WFC3/IR	15117	Steinhardt, Charles L.
	F555W, F814W	WFC3/UVIS	12880	Riess, Adam
	F625W, F814W	WFC3/UVIS	13790	Rodney, Steve
	F275W, F336W	WFC3/UVIS	14209	Siana, Brian
	F225W	WFC3/UVIS	15940	Ribeiro, Bruno
	F275W	WFC3/UVIS	16741	Galbany, Lluís
MACSJ0416.10-2403	F435W, F475W, F606W, F625W	ACS/WFC	12459	Postman, Marc
	F775W, F814W, F850LP	ACS/WFC	12459	Postman, Marc
	F606W, F814W	ACS/WFC	13386	Rodney, Steve
	F814W	ACS/WFC	13459	Treu, Tommaso L.
	F435W, F606W, F814W	ACS/WFC	13496	Lotz, Jennifer
	F435W, F606W	ACS/WFC	14209	Siana, Brian
	F606W, F814W	ACS/WFC	15117	Steinhardt, Charles L.
	F606W, F814W	ACS/WFC	15936	Kelly, Patrick
	F475W	ACS/WFC	15940	Ribeiro, Bruno
	F606W, F814W	ACS/WFC	16278	Kelly, Patrick
	F105W, F110W, F125W, F140W, F160W	WFC3/IR	12459	Postman, Marc
	F105W, F125W, F160W	WFC3/IR	13386	Rodney, Steve
	F105W, F140W	WFC3/IR	13459	Treu, Tommaso L.
	F105W, F125W, F140W, F160W	WFC3/IR	13496	Lotz, Jennifer
	F105W, F125W, F160W	WFC3/IR	15117	Steinhardt, Charles L.
	F105W	WFC3/IR	16729	Kelly, Patrick
	F225W, F275W, F336W, F390W	WFC3/UVIS	12459	Postman, Marc
	F275W, F336W	WFC3/UVIS	14209	Siana, Brian
	F225W	WFC3/UVIS	15940	Ribeiro, Bruno
	F606W	WFC3/UVIS	16729	Kelly, Patrick
A2744	F435W, F606W, F814W	ACS/WFC	11689	Dupke, Renato A.
	F606W, F814W	ACS/WFC	13386	Rodney, Steve
	F435W, F606W	ACS/WFC	13389	Siana, Brian
	F814W	ACS/WFC	13459	Treu, Tommaso L.
	F435W, F606W, F814W	ACS/WFC	13495	Lotz, Jennifer
	F606W, F814W	ACS/WFC	15117	Steinhardt, Charles L.
	F475W	ACS/WFC	15940	Ribeiro, Bruno
	F606W, F775W	ACS/WFC	17231	Treu, Tommaso L.
	F105W, F125W, F160W	WFC3/IR	13386	Rodney, Steve
	F105W, F140W	WFC3/IR	13459	Treu, Tommaso L.
	F105W, F125W, F140W, F160W	WFC3/IR	13495	Lotz, Jennifer
	F105W, F125W, F160W	WFC3/IR	15117	Steinhardt, Charles L.
	F275W, F336W	WFC3/UVIS	13389	Siana, Brian
	F225W	WFC3/UVIS	15940	Ribeiro, Bruno
MACSJ1149.5+2223	F814W	ACS/WFC	10493	Gal-Yam, Avishay
	F435W, F475W, F606W, F625W	ACS/WFC	12068	Postman, Marc
	F775W, F850LP	ACS/WFC	12068	Postman, Marc
	F435W, F606W	ACS/WFC	13389	Siana, Brian
	F814W	ACS/WFC	13459	Treu, Tommaso L.

**Table 8**  
(Continued)

Field	Filters	Instrument	Proposal ID	Proposal PI
ALCS: Hubble Frontier Fields				
	F435W, F606W, F814W	ACS/WFC	13504	Lotz, Jennifer
	F606W, F814W	ACS/WFC	13790	Rodney, Steve
	F606W, F814W	ACS/WFC	14199	Kelly, Patrick
	F435W, F475W, F606W, F814W	ACS/WFC	14208	Rodney, Steve
	F606W, F814W	ACS/WFC	14872	Kelly, Patrick
	F606W, F814W	ACS/WFC	15117	Steinhardt, Charles Louis
	F606W, F814W	ACS/WFC	15308	Gonzalez, Anthony Herman
	F606W, F814W	ACS/WFC	15936	Kelly, Patrick
	F475W	ACS/WFC	15940	Ribeiro, Bruno
	F775W	ACS/WFC	9480	Rhodes, Jason D.
	F775W	ACS/WFC	9584	Sparks, William B.
	F555W, F814W	ACS/WFC	9722	Ebeling, Harald
	F105W, F110W, F125W, F140W, F160W	WFC3/IR	12068	Postman, Marc
	F105W, F140W	WFC3/IR	13459	Treu, Tommaso L.
	F105W, F125W, F140W, F160W	WFC3/IR	13504	Lotz, Jennifer
	F105W, F125W, F140W, F160W	WFC3/IR	13767	Trenti, Michele
	F105W, F125W, F160W	WFC3/IR	13790	Rodney, Steve
	F125W, F160W	WFC3/IR	14041	Kelly, Patrick
	F105W, F125W, F160W	WFC3/IR	14199	Kelly, Patrick
	F105W, F125W, F160W	WFC3/IR	14208	Rodney, Steve
	F125W, F160W	WFC3/IR	14528	Kelly, Patrick
	F110W, F125W, F160W	WFC3/IR	14872	Kelly, Patrick
	F110W	WFC3/IR	14922	Kelly, Patrick
	F105W, F125W, F160W	WFC3/IR	15117	Steinhardt, Charles L.
	F105W, F160W	WFC3/IR	15308	Gonzalez, Anthony Herman
	F225W, F275W, F336W, F390W	WFC3/UVIS	12068	Postman, Marc
	F275W, F336W	WFC3/UVIS	13389	Siana, Brian
	F814W	WFC3/UVIS	13790	Rodney, Steve
	F606W, F814W	WFC3/UVIS	14041	Kelly, Patrick
	F275W, F336W, F606W	WFC3/UVIS	14199	Kelly, Patrick
	F336W	WFC3/UVIS	14208	Rodney, Steve
	F606W	WFC3/UVIS	14528	Kelly, Patrick
	F606W	WFC3/UVIS	14872	Kelly, Patrick
	F606W	WFC3/UVIS	14922	Kelly, Patrick
	F225W	WFC3/UVIS	15940	Ribeiro, Bruno
ALCS: CLASH				
A383	F435W, F475W, F606W	ACS/WFC	12065	Postman, Marc
	F625W, F775W, F814W, F850LP	ACS/WFC	12065	Postman, Marc
	F606W, F850LP	ACS/WFC	12099	Riess, Adam
	F105W, F110W, F125W, F140W, F160W	WFC3/IR	12065	Postman, Marc
	F105W, F160W	WFC3/IR	12099	Riess, Adam
	F105W, F125W, F160W	WFC3/IR	12360	Perlmutter, Saul
	F225W, F275W, F336W	WFC3/UVIS	12065	Postman, Marc
	F390W, F814W	WFC3/UVIS	12065	Postman, Marc
	F814W	WFC3/UVIS	12099	Riess, Adam
MACS1206.2-0847	F606W	ACS/WFC	10491	Ebeling, Harald
	F435W, F475W, F606W, F625W	ACS/WFC	12069	Postman, Marc
	F775W, F814W, F850LP	ACS/WFC	12069	Postman, Marc
	F105W, F110W, F125W, F140W, F160W	WFC3/IR	12069	Postman, Marc
	F110W	WFC3/IR	16729	Kelly, Patrick
	F225W, F275W, F336W, F390W	WFC3/UVIS	12069	Postman, Marc
	F336W	WFC3/UVIS	15271	Ferguson, Harry C.
	F606W	WFC3/UVIS	16729	Kelly, Patrick
MACS1423.8+2404	F814W	ACS/WFC	10493	Gal-Yam, Avishay
	F435W, F475W, F606W, F775W, F850LP	ACS/WFC	12790	Postman, Marc
	F850LP	ACS/WFC	13063	Riess, Adam
	F606W, F775W, F814W, F850LP	ACS/WFC	13386	Rodney, Steve

**Table 8**  
(Continued)

Field	Filters	Instrument	Proposal ID	Proposal PI
ALCS: CLASH				
	F814W	ACS/WFC	13459	Treu, Tommaso L.
	F814W	ACS/WFC	15444	Barth, Aaron J.
	F435W, F606W	ACS/WFC	16667	Bradac, Marusa
	F555W, F814W	ACS/WFC	9722	Ebeling, Harald
	F105W, F110W, F125W, F140W, F160W	WFC3/IR	12790	Postman, Marc
	F125W, F160W	WFC3/IR	13063	Riess, Adam
	F105W, F125W, F140W, F160W	WFC3/IR	13386	Rodney, Steve
	F105W, F140W	WFC3/IR	13459	Treu, Tommaso L.
	F225W, F275W, F336W, F390W	WFC3/UVIS	12790	Postman, Marc
	F606W	WFC3/UVIS	13386	Rodney, Steve
	F438W, F606W	WFC3/UVIS	16667	Bradac, Marusa
MACS1931.8-2635	F435W, F475W, F606W, F625W	ACS/WFC	12456	Postman, Marc
	F775W, F814W, F850LP	ACS/WFC	12456	Postman, Marc
	F105W, F110W, F125W, F140W, F160W	WFC3/IR	12456	Postman, Marc
	F225W, F275W, F336W, F390W	WFC3/UVIS	12456	Postman, Marc
RXJ 1347-1145	F475W, F814W, F850LP	ACS/WFC	10492	Erben, Thomas
	F814W	ACS/WFC	11591	Kneib, Jean-Paul Richard
	F435W, F606W, F625W, F775W, F850LP	ACS/WFC	12104	Postman, Marc
	F814W	ACS/WFC	13459	Treu, Tommaso L.
	F110W, F160W	WFC3/IR	11591	Kneib, Jean-Paul Richard
	F105W, F110W, F125W, F140W, F160W	WFC3/IR	12104	Postman, Marc
	F105W, F160W	WFC3/IR	13386	Rodney, Steve
	F105W, F140W	WFC3/IR	13459	Treu, Tommaso L.
	F110W	WFC3/IR	16729	Kelly, Patrick
	F225W, F275W, F336W, F390W	WFC3/UVIS	12104	Postman, Marc
	F606W	WFC3/UVIS	13386	Rodney, Steve
	F606W	WFC3/UVIS	16729	Kelly, Patrick
MACS1311.0-0310	F435W, F475W, F606W, F625W	ACS/WFC	12789	Postman, Marc
	F775W, F814W, F850LP	ACS/WFC	12789	Postman, Marc
	F105W, F110W, F125W, F140W, F160W	WFC3/IR	12789	Postman, Marc
	F225W, F275W, F336W, F390W	WFC3/UVIS	12789	Postman, Marc
MACS1115.9+0129	F606W	ACS/WFC	10491	Ebeling, Harald
	F435W, F475W, F606W, F625W	ACS/WFC	12453	Postman, Marc
	F775W, F814W, F850LP	ACS/WFC	12453	Postman, Marc
	F105W, F110W, F125W, F140W, F160W	WFC3/IR	12453	Postman, Marc
	F110W	WFC3/IR	16729	Kelly, Patrick
	F225W, F275W, F336W, F390W	WFC3/UVIS	12453	Postman, Marc
	F606W	WFC3/UVIS	16729	Kelly, Patrick
MACS0429.6-0253	F435W, F475W, F606W, F625W	ACS/WFC	12788	Postman, Marc
	F775W, F814W, F850LP	ACS/WFC	12788	Postman, Marc
	F105W, F110W, F125W, F140W, F160W	WFC3/IR	12788	Postman, Marc
	F225W, F275W, F336W, F390W	WFC3/UVIS	12788	Postman, Marc
	F225W, F336W	WFC3/UVIS	16173	Tremblay, Grant R.
RXJ2129.7+0005	F606W	ACS/WFC	10588	Brotherton, Michael S.
	F435W, F475W, F606W, F625W	ACS/WFC	12457	Postman, Marc
	F775W, F814W, F850LP	ACS/WFC	12457	Postman, Marc
	F555W, F775W, F850LP	ACS/WFC	12461	Riess, Adam
	F105W, F110W, F125W, F140W, F160W	WFC3/IR	12457	Postman, Marc
	F105W, F125W, F160W	WFC3/IR	12461	Riess, Adam
	F225W, F275W, F336W, F390W	WFC3/UVIS	12457	Postman, Marc
MACS0329.7-0211	F435W, F475W, F606W, F625W	ACS/WFC	12452	Postman, Marc
	F775W, F814W, F850LP	ACS/WFC	12452	Postman, Marc
	F105W, F110W, F125W, F140W, F160W	WFC3/IR	12452	Postman, Marc
	F225W, F275W, F336W, F390W	WFC3/UVIS	12452	Postman, Marc
MACS2129.4-074	F814W	ACS/WFC	10493	Gal-Yam, Avishay
	F775W, F814W, F850LP	ACS/WFC	12099	Riess, Adam

**Table 8**  
(Continued)

Field	Filters	Instrument	Proposal ID	Proposal PI
ALCS: CLASH				
	F435W, F475W, F606W, F625W, F775W	ACS/WFC	12100	Postman, Marc
	F850LP	ACS/WFC	12100	Postman, Marc
	F606W, F814W	ACS/WFC	13386	Rodney, Steve
	F814W	ACS/WFC	13459	Treu, Tommaso L.
	F814W	ACS/WFC	13790	Rodney, Steve
	F555W, F814W	ACS/WFC	9722	Ebeling, Harald
	F125W, F160W	WFC3/IR	12099	Riess, Adam
	F105W, F110W, F125W, F140W, F160W	WFC3/IR	12100	Postman, Marc
	F105W, F125W, F140W, F160W	WFC3/IR	13386	Rodney, Steve
	F105W, F140W	WFC3/IR	13459	Treu, Tommaso L.
	F125W, F160W	WFC3/IR	13790	Rodney, Steve
	F140W	WFC3/IR	15663	Akhshik, Mohammad
	F225W, F275W, F336W	WFC3/UVIS	12099	Riess, Adam
	F225W, F275W, F336W, F390W	WFC3/UVIS	12100	Postman, Marc
A209	F435W, F475W, F606W, F625W	ACS/WFC	12451	Postman, Marc
	F775W, F814W, F850LP	ACS/WFC	12451	Postman, Marc
	F105W, F110W, F125W, F140W, F160W	WFC3/IR	12451	Postman, Marc
	F225W, F275W, F336W, F390W	WFC3/UVIS	12451	Postman, Marc
ALCS: RELICS				
RXCJ0032.1+1808	F606W, F814W	ACS/WFC	12166	Ebeling, Harald
	F435W, F606W, F814W	ACS/WFC	14096	Coe, Dan
	F105W, F125W, F140W, F160W	WFC3/IR	14096	Coe, Dan
A2537	F435W, F814W	ACS/WFC	14096	Coe, Dan
	F606W	ACS/WFC	9270	Allen, Steven W.
	F775W	ACS/WFC	9575	Sparks, William B.
	F775W	ACS/WFC	9984	Rhodes, Jason D.
	F105W, F125W, F140W, F160W	WFC3/IR	14096	Coe, Dan
A3192	F606W	ACS/WFC	10881	Smith, Graham
	F435W, F606W, F814W	ACS/WFC	12313	Ebeling, Harald
	F105W, F125W, F140W, F160W	WFC3/IR	14096	Coe, Dan
MACSJ0553.4-3342	F435W, F606W, F814W	ACS/WFC	12362	Ebeling, Harald
	F105W, F125W, F140W, F160W	WFC3/IR	14096	Coe, Dan
RXC J0600.1-2007	F814W	ACS/WFC	12884	Ebeling, Harald
	F435W, F606W, F814W	ACS/WFC	14096	Coe, Dan
	F105W, F125W, F140W, F160W	WFC3/IR	14096	Coe, Dan
RXC J0949.8+1707	F606W	ACS/WFC	10491	Ebeling, Harald
	F814W	ACS/WFC	12166	Ebeling, Harald
	F435W, F606W, F814W	ACS/WFC	14096	Coe, Dan
	F110W	WFC3/IR	14047	Reines, Amy E.
	F105W, F125W, F140W, F160W	WFC3/IR	14096	Coe, Dan
MACSJ0257.1-2325	F814W	ACS/WFC	10493	Gal-Yam, Avishay
	F814W	ACS/WFC	10793	Gal-Yam, Avishay
	F435W	ACS/WFC	14096	Coe, Dan
	F555W, F814W	ACS/WFC	9722	Ebeling, Harald
	F105W, F125W, F140W, F160W	WFC3/IR	14096	Coe, Dan
A2163	F435W, F606W, F814W	ACS/WFC	12253	Clowe, Douglas
	F105W, F125W, F140W, F160W	WFC3/IR	14096	Coe, Dan
PLCK G171.9-40.7	F435W, F606W, F814W	ACS/WFC	14096	Coe, Dan
	F105W, F125W, F140W, F160W	WFC3/IR	14096	Coe, Dan
SMACSJ0723.3-7327	F606W	ACS/WFC	12166	Ebeling, Harald
	F814W	ACS/WFC	12884	Ebeling, Harald

**Table 8**  
(Continued)

Field	Filters	Instrument	Proposal ID	Proposal PI
ALCS: RELICS				
	F435W, F606W, F814W	ACS/WFC	14096	Coe, Dan
	F105W, F125W, F140W, F160W	WFC3/IR	14096	Coe, Dan
MACSJ0035.4-2015	F606W	ACS/WFC	10491	Ebeling, Harald
	F814W	ACS/WFC	12884	Ebeling, Harald
	F435W, F606W, F814W	ACS/WFC	14096	Coe, Dan
	F105W, F125W, F140W, F160W	WFC3/IR	14096	Coe, Dan
MACSJ0417.5-1154	F814W	ACS/WFC	12009	von der Linden, Anja
	F435W	ACS/WFC	14096	Coe, Dan
	F435W, F606W	ACS/WFC	16667	Bradac, Marusa
	F105W, F125W, F140W, F160W	WFC3/IR	14096	Coe, Dan
	F606W	WFC3/UVIS	12009	von der Linden, Anja
	F438W, F606W, F814W	WFC3/UVIS	16667	Bradac, Marusa
	F606W	WFC3/UVIS	16863	Anderson, Jay
MACSJ0159.8-0849	F606W	ACS/WFC	12166	Ebeling, Harald
	F435W, F606W, F814W	ACS/WFC	14096	Coe, Dan
	F105W, F125W, F140W, F160W	WFC3/IR	14096	Coe, Dan
ACT-CLJ0102-49151	F606W, F814W	ACS/WFC	12477	High, Fredrick W.
	F625W, F775W, F850LP	ACS/WFC	12755	Hughes, John P.
	F435W	ACS/WFC	14096	Coe, Dan
	F606W	ACS/WFC	14153	Hughes, John P.
	F105W, F125W, F140W, F160W	WFC3/IR	14096	Coe, Dan
	F140W	WFC3/IR	16773	Glazebrook, Karl
AbellS295	F435W, F606W, F814W	ACS/WFC	13514	Pacaud, Florian
	F105W, F125W, F140W, F160W	WFC3/IR	14096	Coe, Dan
	F105W	WFC3/IR	16729	Kelly, Patrick
	F606W	WFC3/UVIS	16729	Kelly, Patrick
RXC J2211.7-0350	F606W	ACS/WFC	12166	Ebeling, Harald
	F435W, F606W, F814W	ACS/WFC	14096	Coe, Dan
	F105W, F125W, F140W, F160W	WFC3/IR	14096	Coe, Dan
	F475W	WFC3/UVIS	11565	Lepine, Sebastien

computed by EAZY. The units of the photometry are in microjanskys, which corresponds to the magnitude in the AB system of  $23.9 - 2.5 \log_{10}(f_{\nu} / \mu\text{Jy})$ . In Table 6 we provide the encircled energy corrections for all HST filters within a  $D = 0''.7$  aperture. For each field we also compute the median  $1\sigma$  depth from uncertainty on the total photometry. These values are presented in Table 7. All HST data used in this work are listed in Table 8. The IRAC data used in this work was collected during the following programs: HFF (Lotz et al. 2019), RELICS (Bradac et al. 2020), and CLASH (CLASH Team 2020).

## Appendix B Quality and Consistency Verification

In this section we present a comparison between HST broadband photometry measurements and low-resolution IRAC model photometry to the publicly available catalogs covering the ALCS fields. These include the HFF-DeepSpace and ASTRODEEP catalogs in the HFF (Merlin et al. 2016a; Di Criscienzo et al. 2017; Shipley et al. 2018), which most closely match our photometric baseline, and also process the IRAC

photometry. In addition we also carry out a comparison between our photometry and the Molino et al. (2017) catalogs, in the CLASH fields, albeit only for HST data. The comparison is carried out on a per-filter basis, and also includes the difference between the derived colors. Where appropriate, we also contrast the area-weighted number counts in the detection bands.

### B.1. Hubble Frontier Fields-DeepSpace

The HFF-DeepSpace multiwavelength photometric catalog is presented in Shipley et al. (2018). The catalog focuses on the six Frontier fields, plus the associated parallels. Our overlap with HFF-DeepSpace includes all cluster and parallel regions apart from MACSJ0717.5+3745, which we will exclude from our comparison. The UV-optical photometric catalog consists of up to 17 filters with HST/ACS and HST/WFC3, Very Large Telescope/HAWK-I  $K_s$  filter, and the (post-cryogenic) IRAC 3.6  $\mu\text{m}$  and 4.5  $\mu\text{m}$  data, plus the archival IRAC 5.8  $\mu\text{m}$  and 8  $\mu\text{m}$  measurements, where available.

The HFF-DeepSpace methodology starts with recombination of all the background-subtracted HST exposures from different

epochs, and performing an initial image cleaning from artifacts and cosmic rays. After that, for each cluster field they follow the Ferrarese et al. (2006) method to model and subtract out BCGs and the ICL from each field, performing additional background cleaning on the BCG-subtracted mosaics. This procedure allows one to identify more objects magnified by the gravitational potential of the cluster members, and to assign the correct flux values to galaxies that are located close to the cluster on the sky.

After the BCGs have been subtracted, all shorter-wavelength mosaics are then PSF-matched to the F160W band. The mosaics for all available HST filters are then combined into a single weighted mean detection image. The source detection itself is then performed on the resultant image by using SEXTRACTOR, generally following the methodology described in Skelton et al. (2014). The HST aperture photometry extraction within a diameter of  $0''.7$  is then performed on the detection and individual PSF-matched HST images, and the correction to the total flux density is calculated from the curves of growth.

Low-resolution IRAC photometry is extracted by using MOPHONGO (Labbé et al. 2013, 2015), a code developed to process longer-wavelength bands, specifically focusing on potentially blended objects. Similarly to GOLFIR, the high-resolution detection image is convolved with a low-resolution kernel and used as a model to fit the IRAC photometry. However, these models are not used to extract the flux density but rather to correct for the possible contamination from the neighboring sources, with the IRAC flux densities themselves being extracted from  $3''.0$  apertures. Additional flux density corrections are performed by using the PSF curves of growth.

Apart from the aperture corrections, the measured flux densities of Shipley et al. (2018) have undergone a number of additional modifications with the aim of providing the best possible results during SED fitting. These include the zero-point and the Milky Way extinction corrections. The values presented in our photometric catalog do not incorporate such corrections, and therefore we had to de-apply them, as specified in the Shipley et al. (2018) catalog documentation. Our knowledge of galaxy SEDs is still limited, especially as we move into the high- $z$  universe, thus preventing us from accurately calculating the zero-point corrections (see, e.g., Brown et al. 2014), with the template error function largely alleviating these effects, however not in their entirety (Brammer et al. 2008). Moreover, calculating extinction corrections would largely depend on the the adopted models, introducing unwanted shifts if not done carefully. Due to this, although both the zero-point and Milky Way corrections are largely inconsequential ( $\mathcal{O} \sim 2\%$ ), we take great care to convert total flux densities back to their original values to carry out a robust and unbiased photometry comparison without these corrections. The flux densities presented in the Shipley et al. (2018) catalog have been additionally normalized to  $AB = 25$ , rather than  $AB = 23.9$ , which we also take into account when comparing the results.

The total combined science area of the CHARGE/GOLFIR HST and IRAC data in our catalog, after removing masked regions, is equal to  $312.6 \text{ arcmin}^2$ , roughly double the size of the HFF-DeepSpace coverage of  $136.7 \text{ arcmin}^2$ . This results in a higher number of objects recovered in our work, which after removing potential spurious and masked sources totals to 125,947 across all five Frontier Fields,  $\times 2.3$  larger than the

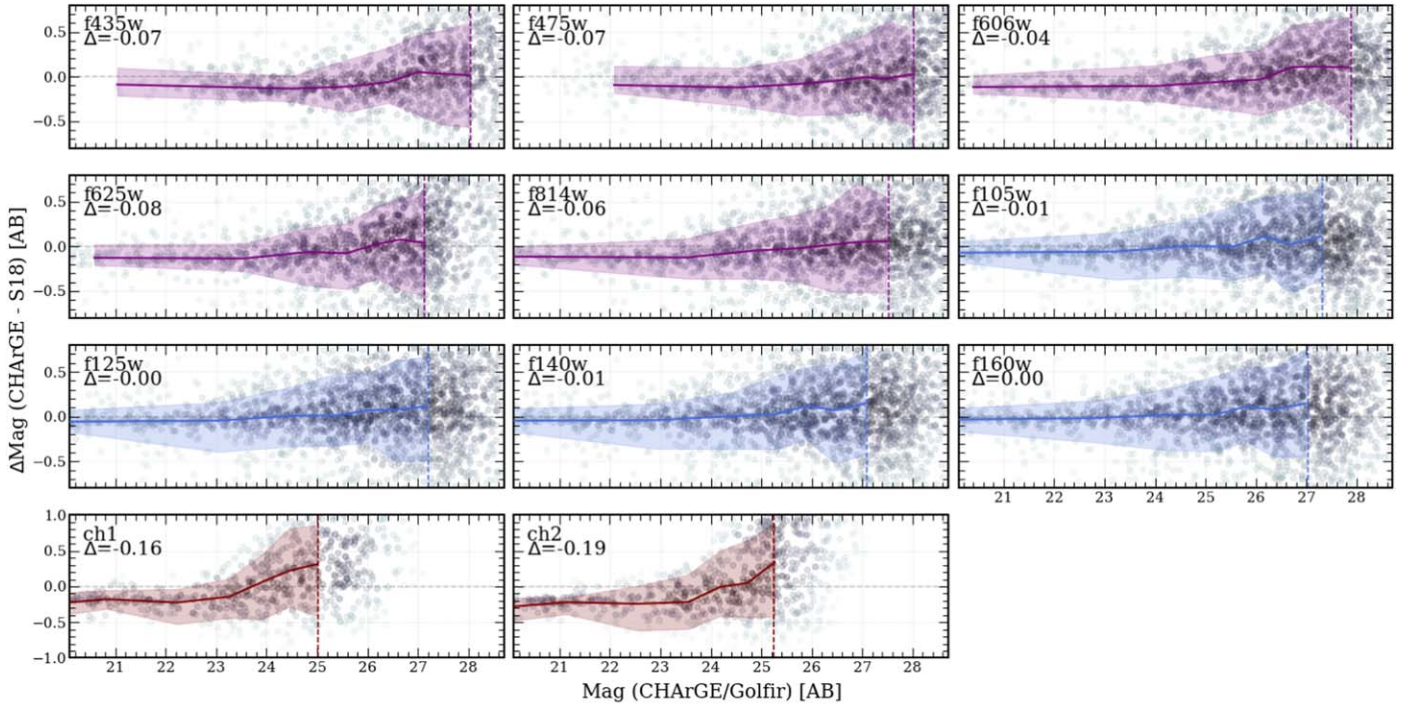
use\_phot HFF-DeepSpace sample, which numbers 55,579 objects. To perform the photometric comparison between the two catalogs, we only focus on the regions where the two overlap. However, even for the parts where our data cover the same area, the CHARGE images include new exposures, mainly from the BUFFALO survey (Steinhardt et al. 2020), not originally present in the Shipley et al. (2018) analysis, particularly on the edges of the old mosaic. Therefore, blind matching of all available sources would be inappropriate for a fair photometry comparison, with the variation in depth potentially introducing some deleterious effects. Instead, we focus on the central parts of both the cluster (clu) and parallel (par) regions of all five Frontier Fields, where the coverage is deepest and uniform for both catalogs. In addition, as mentioned in Section 3, we do not model or subtract the BCG when computing the photometry, therefore focusing only on the central area will allow us to contrast how BCG modeling affects the final measured flux densities. We have used a  $1''.0$  matching radius, and find that the average astrometric offset between the two catalogs is equal to  $\sim 0''.12$ , which we have corrected for.

In Figure 10 we show a comparison between ALCS CHARGe/GOLFIR and HFF-DeepSpace catalogs for the A370 field. We carry out the comparison for individual filters and colors separately for the cluster and parallel parts, depending on the availability of the photometry. For HST photometry the agreement is largely good to excellent. The median offsets vary with instrument, from  $-0.06 \text{ mag}$  in HST/ACS to  $0.02 \text{ mag}$  in HST/WFC3 filters. Our flux densities are consistently brighter; however, this does not seem to stem from the lack of BCG subtraction, but rather PSF-matching performed on all bands apart from F160W, where our median difference is zero. This notion is further reinforced by the fact that the disparity between flux densities is larger for ACS filters, where the effects of PSF-matching would be most noticeable. For the longer-wavelength IRAC bands, we however note a much larger offset, of  $-0.17 \text{ mag}$ , both for the cluster and the parallels. In an attempt to understand the discrepancy, we have first compared the science images themselves, by randomly placing 1000 apertures in the mosaics. The extracted flux densities were different by, at most,  $\sim 0.05 \text{ mag}$ , which does not explain the difference that we see in our comparison. We suspect that the discrepancy in the IRAC bands can be attributed to the difference in chosen methodology, specifically the aperture to total flux correction.

Comparison of colors yields even better results for both HST and IRAC bands as it largely ignores any differences caused by PSF-matching the individual bands, and on the aperture to total flux corrections. We show these results in Figure 11, again both for cluster and parallel parts of A370. Apart from the F160W  $-3.6 \mu\text{m}$  color, we find offsets of the order of  $-0.01 \text{ mag}$ . Despite the difference in flux measurements, the agreement between colors indicates that measurements in both catalogs have been executed in a consistent way.

Finally, in the top panel of Figure 12 we show the area-weighted number of objects as a function of their apparent magnitude. The source number counts is one of the basic tests to evaluate and characterize sensitivity-limited samples. The comparison is performed in the same “deep” areas of the A370 field, for two representative ACS and WFC3 filters. We do not carry out the same analysis for the IRAC bands, as the flux offsets are too large to compare the number counts in a

## abell370: clu



## abell370: par

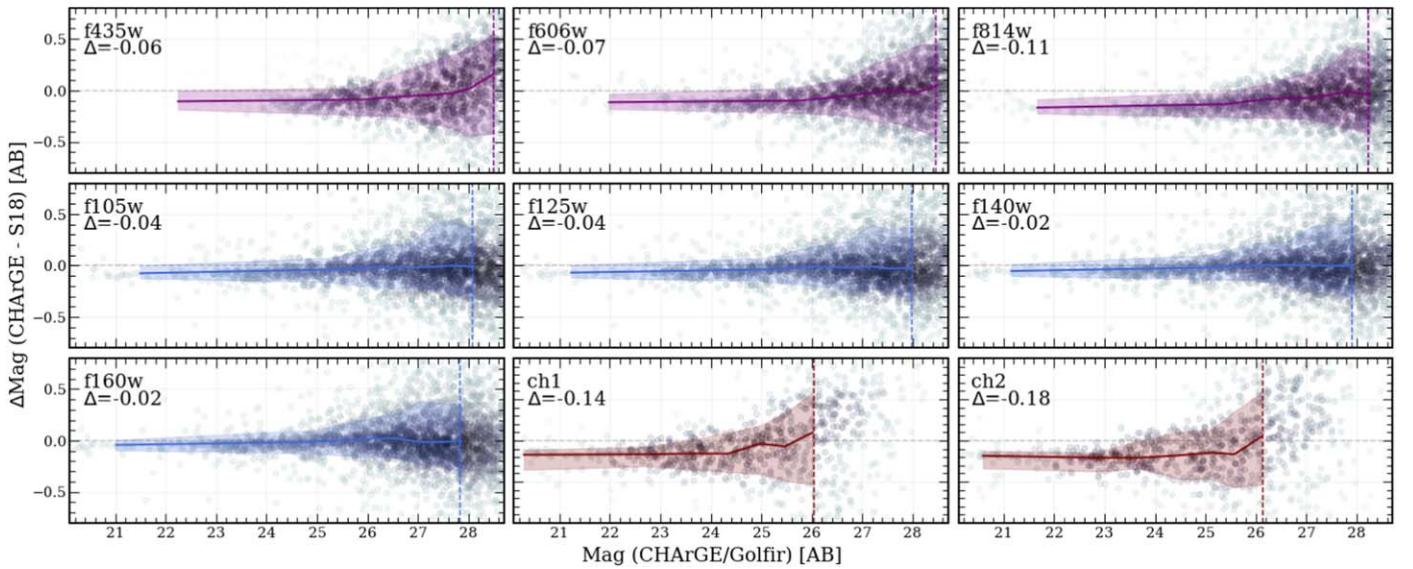


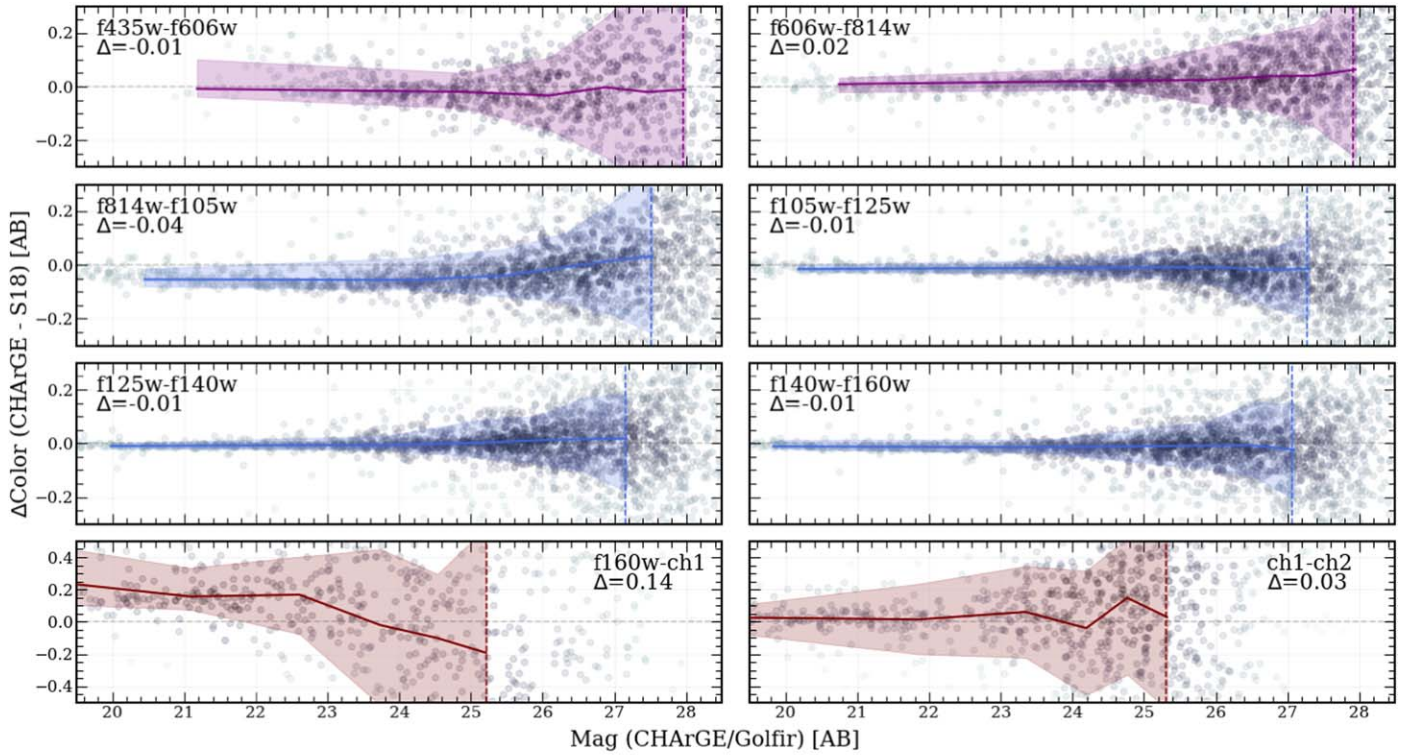
**Figure 10.** The difference between broadband magnitude measured in our catalog and Shipley et al. (2018), for the cluster (top) and parallel (bottom) parts of the A370 field. We only compare the objects in the central part of the field. For clarity, the colors of shaded regions correspond to HST/ACS (purple), HST/WFC3 (blue), and Spitzer/IRAC (maroon). The difference in magnitude  $\Delta\text{Mag}$  is shown by scattered circles, which are colored based on the density of sources around them. The overlaid solid lines correspond to the binned median, which are selected to contain the same amount of objects in each bin. The shaded envelope captures the 68% of points per magnitude bin. The vertical dashed lines correspond to the  $1\sigma$  depth limit for each band. The median  $\Delta\text{Mag}$  for galaxies brighter than the depth limit is shown on each panel.

consistent manner. For this comparison we have only used the “clean” photometry, i.e., the `use_phot=1` flag for HFF-DeepSpace and `n_masked=0` for our data. For each Frontier Field, our detection algorithm recovers roughly 30% more sources, specifically in the faint end. A small fraction of these are expected to be spurious or are a result of overly aggressive deblending of nearby galaxies. The number counts between both catalogs are, however, largely consistent, and show similar depths.

## B.2. ASTRODEEP

For the next comparison we focus on the ASTRODEEP catalog, presented in Merlin et al. (2016a), including the additional data release by Di Criscienzo et al. (2017). The catalogs present the data for the cluster and parallel pointings for four Frontier Fields, A2744, MACSJ0416, MACSJ0717, and MACSJ1149, three of which lie in the ALCS area. The photometric coverage includes 10 bands, covering HST/ACS

## abell370: clu



## abell370: par

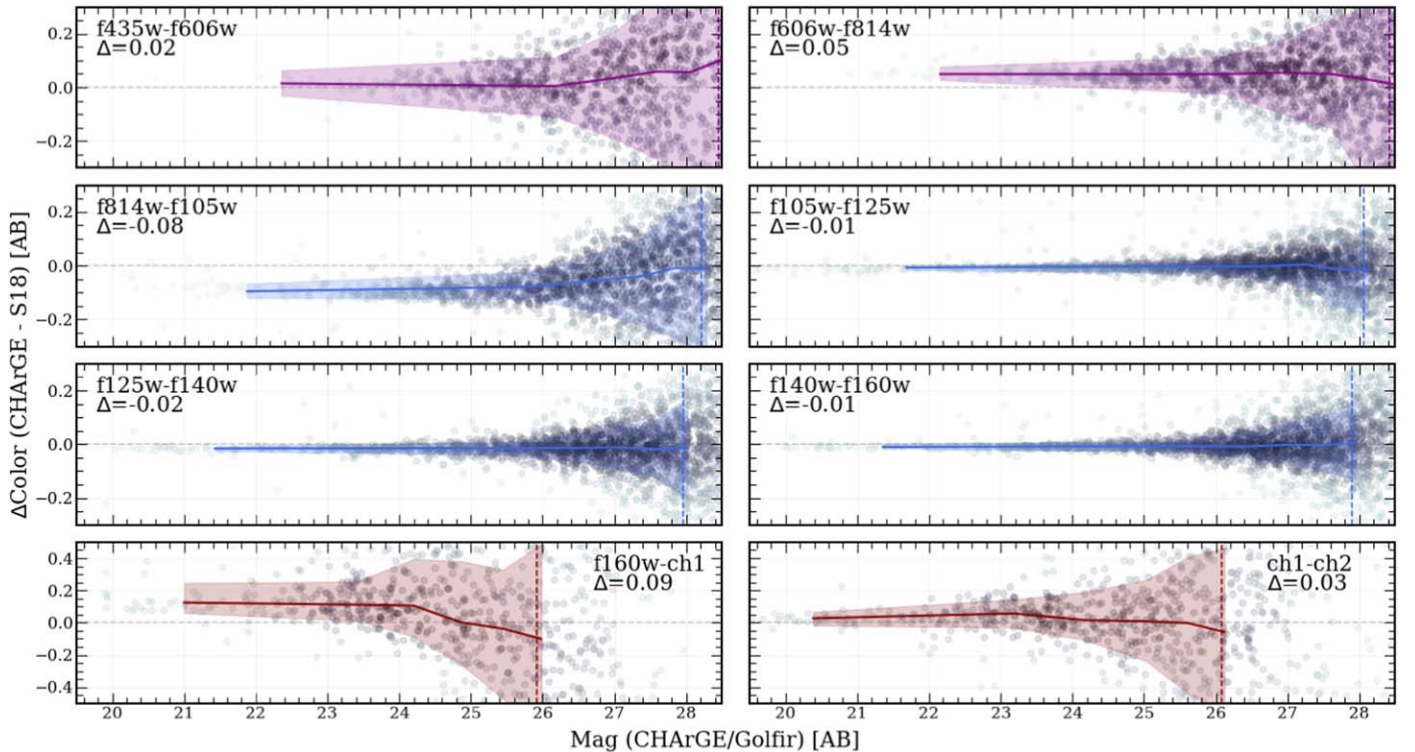


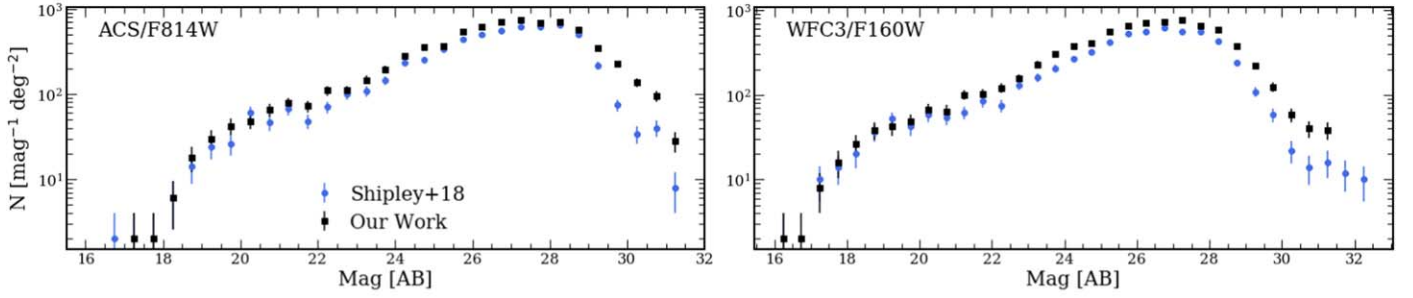
**Figure 11.** The difference between broadband color computed in our catalog and Shipley et al. (2018), for the cluster (top) and parallel (bottom) parts of the A370 field. The colors and symbols are the same as those in Figure 10.

and WFC3, as well as HAWK-I  $K_s$  and IRAC 3.6  $\mu\text{m}$  and 4.5  $\mu\text{m}$  data.

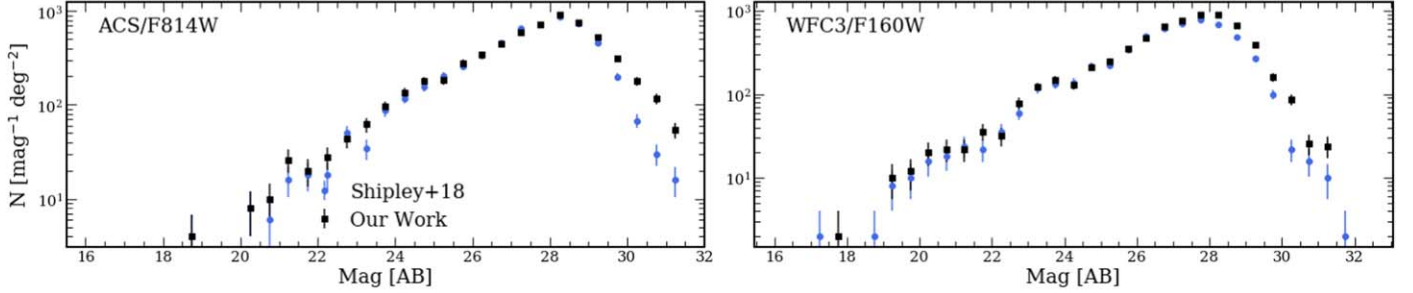
The methodology for the ASTRODEEP catalog is largely similar to the one presented in Shipley et al. (2018). The ICL

and BCGs are modeled and subtracted from the  $H$ -band image by using models from Ferrarese et al. (2006), in conjunction with GALFIT. The HST source detection is performed on a single image, the WFC3 F160W band, by using SEXTRACTOR

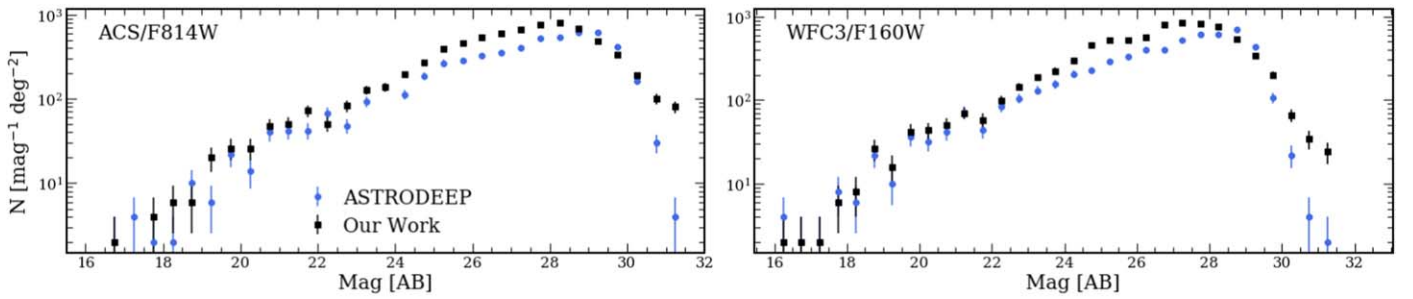
## abell370: clu



## abell370: par



## macs0416: clu



## macs0416: par

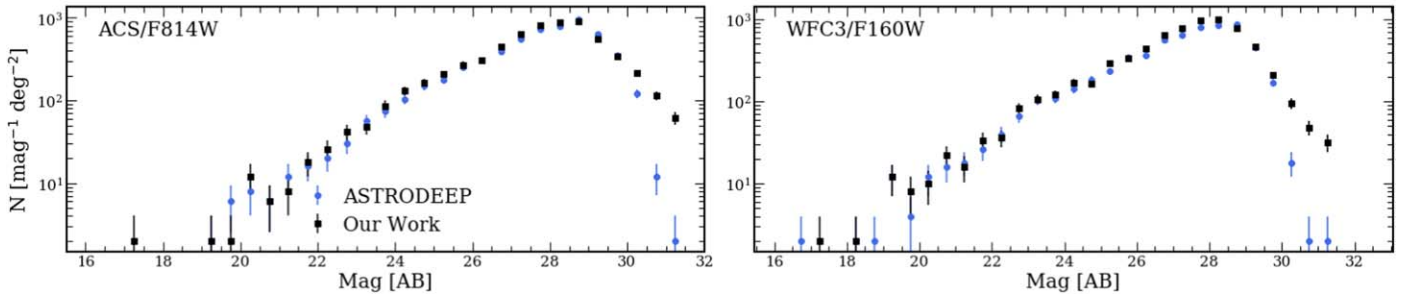


**Figure 12.** Top: The area-normalized number counts in the F814W and F160W filters for the central part of the A370 cluster and parallel fields. We show the number counts for our catalog as black squares, while the Shipley et al. (2018) work is overlotted in blue circles. Bottom: The area-normalized number counts in the F814W and F160W filters for the central part of the MACSJ0416 cluster and parallel fields. We show the number counts for our catalog as black squares, while the ASTRODEEP data are overlotted in blue circles.

in both HOT+COLD modes (see, e.g., Galametz et al. 2013). The authors then use a sequential approach to subtract the ICL and BCGs from all the other cluster images, by using the output of the previous GALFIT run on a redder band, as an initial guess for the bluer one. All of the images are then PSF-matched to the F160W filter, by using a convolution kernel. The final HST photometry is extracted with SEXTRACTOR running in dual mode, to measure the aperture and isophotal fluxes. Total fluxes in the F160W filter are computed from the SEXTRACTOR FLUX\_AUTO parameter. For

other bands the total flux is derived from the scaling of the detection band to all the relevant isophotal colors.

The low-resolution IRAC photometric measurements in the ASTRODEEP catalog follow a method similar to the one outlined in this work and Shipley et al. (2018). The authors use T-PHOT (Merlin et al. 2015), which follows the same methodology as both MOPHONGO and GOLFR, by using high-resolution images convolved with low-resolution PSFs to act as models for the photometric data.

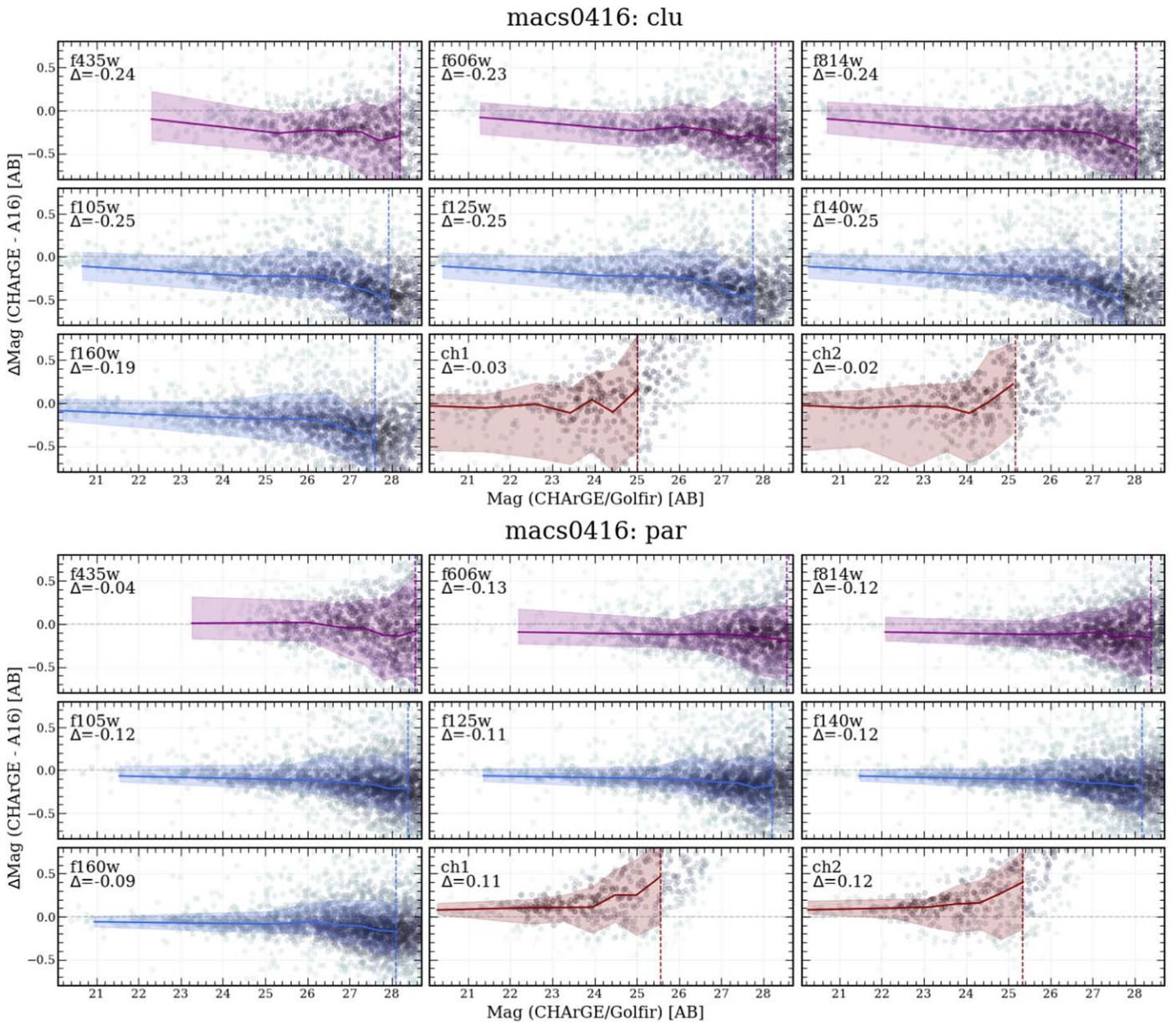


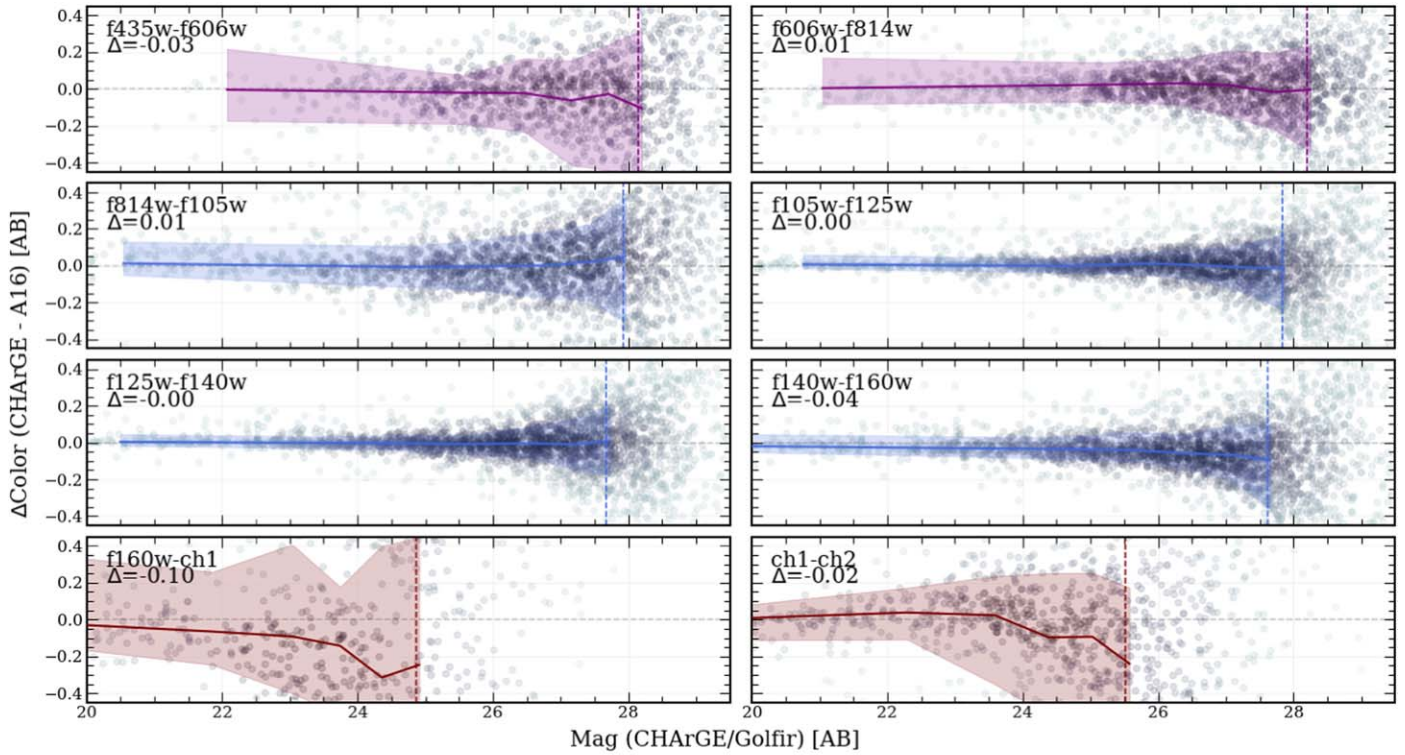
**Figure 13.** The difference between broadband magnitude measured in our catalog and the ASTRODEEP data, for the cluster (top) and parallel (bottom) parts of the MACS0416 field. Symbols and colors are the same as those in Figure 10.

As before, we only compare sources in the central parts of both cluster and parallel fields. For that we used a matching radius of  $1''.0$ . The average astrometric offset between our sources and the ASTRODEEP catalog is  $\sim 0''.22$ . In Figures 13 and 14 we show a comparison between ALCS CHArGe/GOLFIR and ASTRODEEP catalogs for the MACS0416 field. For HST photometry the difference is quite substantial, with a median offset equal to  $-0.21$  mag for the cluster and  $-0.11$  mag for the parallel field, without dependence on the instrument. We suspect that the BCG subtraction is responsible for half of the offset, as the differences in flux are lessened in the parallel field. The fluxes presented in the ASTRODEEP catalog are also extinction corrected, however we believe that this is not a major contributor to the difference that we find. If we ignore the potential effects of BCG subtraction, in most cases the difference between the two catalogs is not a systematic shift but rather an offset increasing at fainter magnitudes. The cause for the flux-

dependent behavior of the offset likely originates from a different aperture used to extract the photometry, and the methodology to convert that flux to total. Unfortunately, we could not carry out the exact flux comparison to the ASTRODEEP catalog, due to the unavailability of documentation regarding the aperture sizes used and total flux corrections. In the IRAC 3.6 and  $4.5\ \mu\text{m}$  filters, however, we find a remarkable agreement, of  $\sim -0.01$  mag, in both cluster and parallel fields. The color comparison, again, yields consistent results, across all HST and IRAC filters. We find an average offset of  $-0.01$  mag for all colors, apart from the F160W  $-3.6\ \mu\text{m}$  color.

Despite large offsets in the ACS and WFC3 bands, we show a number count comparison to the ASTRODEEP catalog in the bottom panel of Figure 12, as the magnitude offsets are too large to yield reasonable results. Notably, however, we again recover roughly 30% more sources, in both cluster and parallel fields on the faint end.

macs0416: clu



macs0416: par

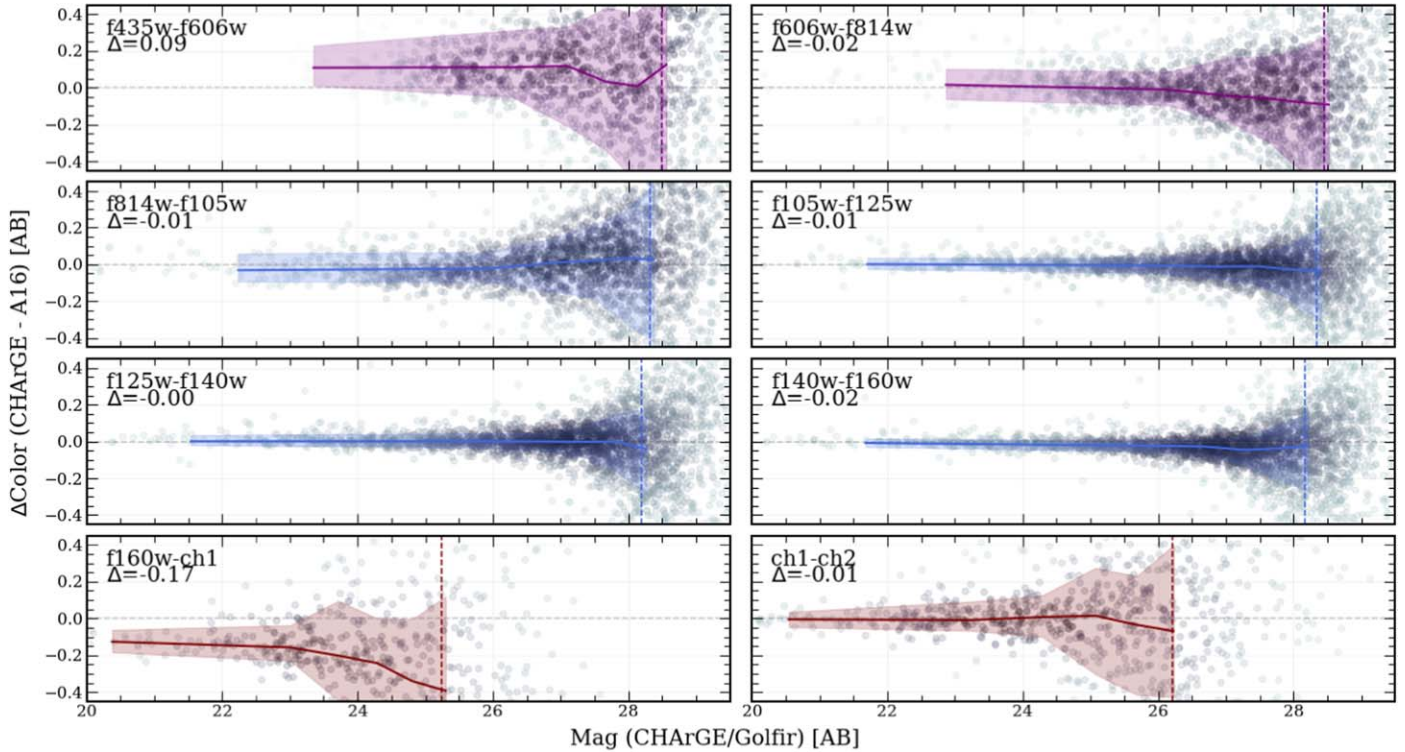


**Figure 14.** The difference between broadband color computed in our catalog compared to ASTRODEEP, for the cluster (top) and parallel (bottom) parts of the MACSJ0416 field. The colors and symbols are the same as those in Figure 10.

*B.3. CLASH Hubble Space Telescope Catalog*

For our final broadband photometry comparison we focus on the CLASH HST catalog presented in Molino et al. (2017). The catalog

contains photometry for 25 massive galaxy clusters in CLASH and overlaps with all 12 ALCS CLASH clusters that we analyzed in our work. The photometric coverage includes 14 bands from HST only, covering HST/ACS and WFC3/UVIS and WFC3/IR.

## All CLASH Fields

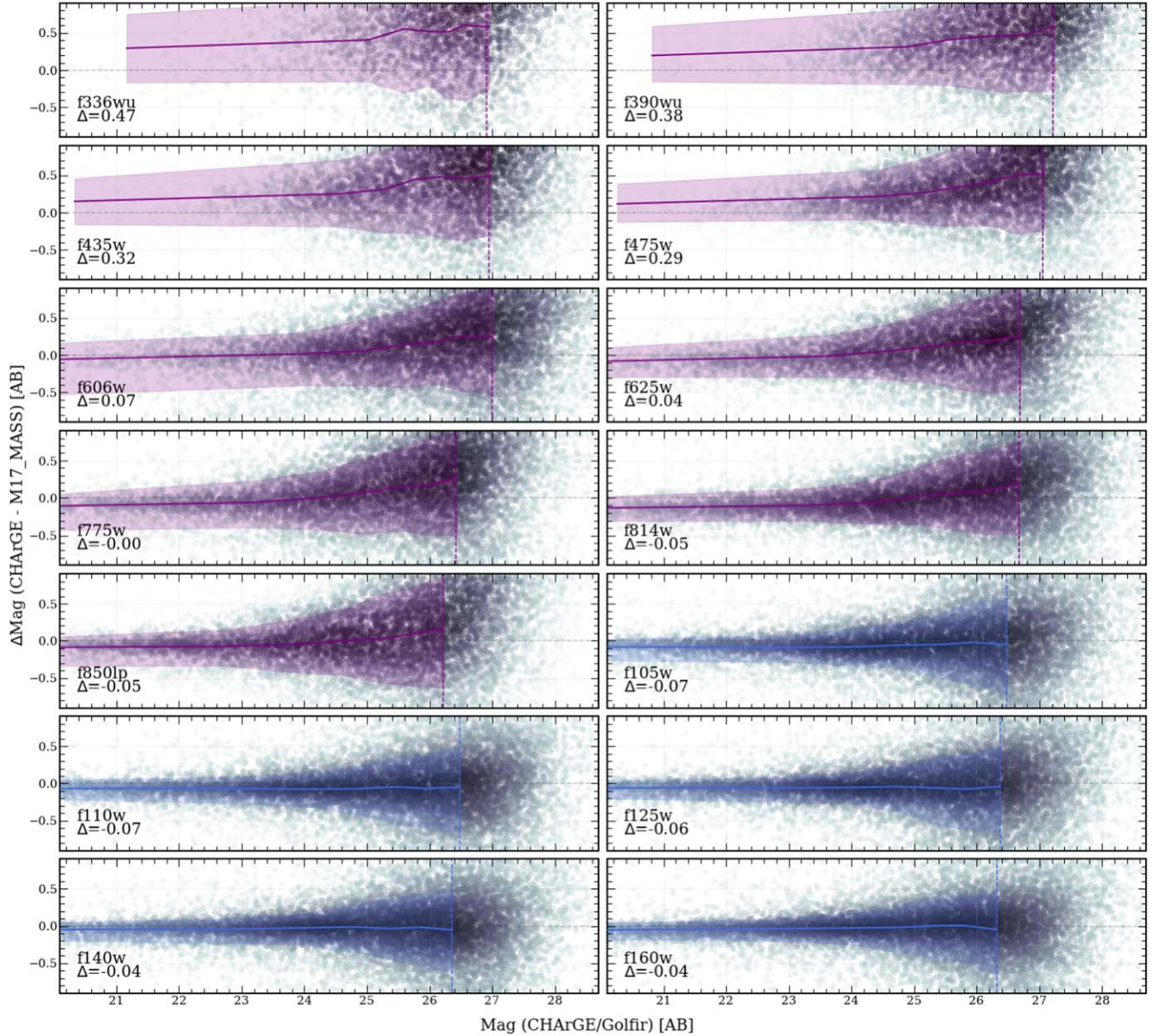


**Figure 15.** The difference between broadband magnitude computed in our catalog compared to CLASH photometric catalog of Molino et al. (2017). The colors and symbols are the same as those in Figure 10.

Similarly to the HFF-DeepSpace and ASTRODEEP catalogs, the ICL and BCG contribution are subtracted from the image. This is achieved by first running SEXTRACTOR on the deep NIR detection images, and then, based on the detected source catalog, modeling and subtraction are performed. After this all short-wavelength mosaics are then PSF-homogenized to the WFC3/IR camera. The photometry itself is performed by using two different sets of apertures, which the authors define as the *restricted* and the *moderate*. In the case of the *restricted* aperture SEXTRACTOR is forced to define the *AUTO* magnitude to the smallest available radius, which does not necessarily integrate all of the light from the galaxy but results in the higher overall S/N. The authors argue that this approach is less sensitive to PSF variations across images and results in more robust recovery of colors, thus yielding more accurate photo-*z* estimates. The latter case of the *moderate* aperture is more similar to our approach

with CHARGE, and relies on increased aperture sizes which aim to integrate all of the light from the galaxy. In contrast to the *restricted* apertures, this approach is argued to be more appropriate for an unbiased extraction of the physical parameters, such as stellar masses, ages, and metallicities. For the purposes of this comparison we will only focus on the photometry extracted from the *moderate* apertures, as this most closely resembles the approach that we undertook in this work.

We match all 12 CLASH fields where CHARGE and the Molino et al. (2017) catalog data overlap, with a  $1''.0$  matching radius. The average astrometric offset computed across 12 fields is equal to  $\sim 0''.18$ . We show the comparison between the broadband photometry for 14 HST filters in Figure 15. We find that the agreement between the two data sets is mostly good, apart from the bluest HST/ACS and UVIS bands. The median offsets are generally consistent across all instruments and vary

## All CLASH Fields

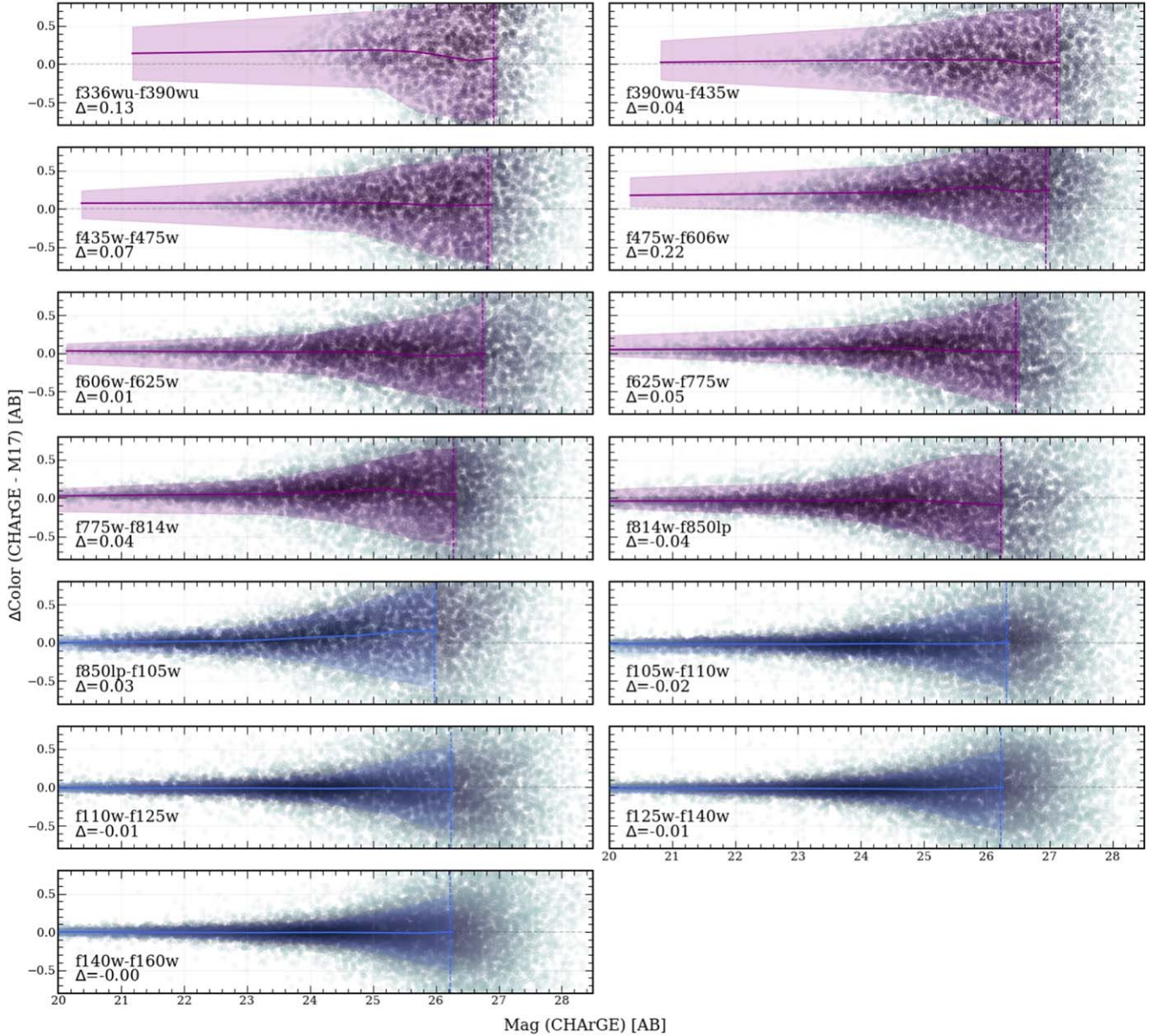


**Figure 16.** The difference between broadband color computed in our catalog compared to CLASH photometric catalog of Molino et al. (2017). The colors and symbols are the same as those in Figure 10.

from  $-0.04$  mag to  $0.07$  mag. For all of the HST/WFC3 and half the HST/ACS our photometry seems to be systematically brighter, which changes toward being fainter when we move toward bluer filters. The offsets become substantially pronounced for the bluest ACS and WFC3/UVIS bands, with medians reaching upwards of  $0.47$ , indicating that our flux density measurements for those bands are  $\sim 1.5\times$  fainter. Similarly to our comparison with the Shipley et al. (2018) data, the fact that this discrepancy only manifests itself in a specific subset of bands indicates that its origins are not coming from the BCG or ICL subtraction. We thus conclude, as before, that the magnitude offsets are coming from the PSF-matching procedure. The moderate aperture sizes described in Molino et al. (2017) are optimized to integrate almost all of the light around the galaxy, where the maximum aperture size is dictated

by a S/N threshold. While some considerations regarding contamination from the neighboring have been made, the convolution of the high-resolution blue ACS and UVIS bands could have had a deleterious effect on the extracted photometry. A color comparison, presented in Figure 16, yields consistent results across the majority of HST bands, and only strongly deviates for the aforementioned bands where the magnitude offsets are also large.

## ORCID iDs

V. Kokorev  <https://orcid.org/0000-0002-5588-9156>  
 G. Brammer  <https://orcid.org/0000-0003-2680-005X>  
 S. Fujimoto  <https://orcid.org/0000-0001-7201-5066>  
 K. Kohno  <https://orcid.org/0000-0002-4052-2394>  
 G. E. Magdis  <https://orcid.org/0000-0002-4872-2294>

F. Valentino  <https://orcid.org/0000-0001-6477-4011>  
 S. Toft  <https://orcid.org/0000-0003-3631-7176>  
 P. Oesch  <https://orcid.org/0000-0001-5851-6649>  
 I. Davidzon  <https://orcid.org/0000-0002-2951-7519>  
 F. E. Bauer  <https://orcid.org/0000-0002-8686-8737>  
 D. Coe  <https://orcid.org/0000-0001-7410-7669>  
 E. Egami  <https://orcid.org/0000-0003-1344-9475>  
 M. Oguri  <https://orcid.org/0000-0003-3484-399X>  
 M. Ouchi  <https://orcid.org/0000-0002-1049-6658>  
 M. Postman  <https://orcid.org/0000-0002-9365-7989>  
 J. Richard  <https://orcid.org/0000-0001-5492-1049>  
 J.-B. Jolly  <https://orcid.org/0000-0002-3405-5646>  
 K. K. Knudsen  <https://orcid.org/0000-0002-7821-8873>  
 F. Sun  <https://orcid.org/0000-0002-4622-6617>  
 J. R. Weaver  <https://orcid.org/0000-0003-1614-196X>  
 Y. Ao  <https://orcid.org/0000-0003-3139-2724>  
 A. J. Baker  <https://orcid.org/0000-0002-7892-396X>  
 L. Bradley  <https://orcid.org/0000-0002-7908-9284>  
 K. I. Caputi  <https://orcid.org/0000-0001-8183-1460>  
 M. Dessauges-Zavadsky  <https://orcid.org/0000-0003-0348-2917>  
 D. Espada  <https://orcid.org/0000-0002-8726-7685>  
 B. Hatsukade  <https://orcid.org/0000-0001-6469-8725>  
 A. M. Koekemoer  <https://orcid.org/0000-0002-6610-2048>  
 A. M. Muñoz Arancibia  <https://orcid.org/0000-0002-8722-516X>  
 K. Shimasaku  <https://orcid.org/0000-0002-2597-2231>  
 H. Umehata  <https://orcid.org/0000-0003-1937-0573>  
 T. Wang  <https://orcid.org/0000-0002-2504-2421>  
 W.-H. Wang  <https://orcid.org/0000-0003-2588-1265>

## References

- Anderson, J., & King, I. R. 2000, *PASP*, 112, 1360  
 Aravena, M., Decarli, R., Walter, F., et al. 2016, *ApJ*, 833, 68  
 Arnouts, S., Le Floch, E., Chevillard, J., et al. 2013, *A&A*, 558, A67  
 Balestra, I., Mercurio, A., Sartoris, B., et al. 2016, *ApJS*, 224, 33  
 Barbary, K. 2016, *JOSS*, 1, 58  
 Berta, S., Lutz, D., Genzel, R., Förster-Schreiber, N. M., & Tacconi, L. J. 2016, *A&A*, 587, A73  
 Bertin, E., & Arnouts, S. 1996, *A&AS*, 117, 393  
 Blanton, M. R., & Roweis, S. 2007, *AJ*, 133, 734  
 Boselli, A., Roehlly, Y., Fossati, M., et al. 2016, *A&A*, 596, A11  
 Bouwens, R. J., Illingworth, G. D., Franx, M., & Ford, H. 2007, *ApJ*, 670, 928  
 Bouwens, R. J., Illingworth, G. D., Oesch, P. A., et al. 2015, *ApJ*, 803, 34  
 Bouwens, R. J., Oesch, P. A., Labbé, I., et al. 2016, *ApJ*, 830, 67  
 Bower, R. G., Lucey, J. R., & Ellis, R. S. 1992, *MNRAS*, 254, 601  
 Bradac, et al. 2020, Spitzer Reionization Lensing Cluster Survey, IPAC, doi:10.26131/IRSA426  
 Bradley, L. D., Zitrin, A., Coe, D., et al. 2014, *ApJ*, 792, 76  
 Brammer, G. 2022, 0, gbrammer/golfir: Software pipeline for model photometry on images with different point spread functions, v1.0, Zenodo, doi:10.5281/zenodo.7149516  
 Brammer, G., & Matharu, J. 2021, gbrammer/grizli: Release 2021, v1.3.2, Zenodo, doi:10.5281/zenodo.5012699  
 Brammer, G. B., van Dokkum, P. G., & Coppi, P. 2008, *ApJ*, 686, 1503  
 Brammer, G. B., Whitaker, K. E., van Dokkum, P. G., et al. 2011, *ApJ*, 739, 24  
 Brown, M. J. I., Moustakas, J., Smith, J. D. T., et al. 2014, *ApJS*, 212, 18  
 Calvi, V., Trenti, M., Stiavelli, M., et al. 2016, *ApJ*, 817, 120  
 Calzetti, D., Armus, L., Bohlin, R. C., et al. 2000, *ApJ*, 533, 682  
 Caminha, G. B., Grillo, C., Rosati, P., et al. 2016, *A&A*, 587, A80  
 Caminha, G. B., Rosati, P., Grillo, C., et al. 2019, *A&A*, 632, A36  
 Carniani, S., Maiolino, R., De Zotti, G., et al. 2015, *A&A*, 584, A78  
 Chabrier, G. 2003, *PASP*, 115, 763  
 CLASH Team 2020, Cluster Lensing And Supernova survey with Hubble, IPAC, doi:10.26131/IRSA408  
 Coe, D., Zitrin, A., Carrasco, M., et al. 2013, *ApJ*, 762, 32  
 Coe, D., Salmon, B., Bradač, M., et al. 2019, *ApJ*, 884, 85  
 Conroy, C., Gunn, J. E., & White, M. 2009, *ApJ*, 699, 486  
 Davidzon, I., Ilbert, O., Laigle, C., et al. 2017, *A&A*, 605, A70  
 Di Criscienzo, M., Merlin, E., Castellano, M., et al. 2017, *A&A*, 607, A30  
 Diego, J. M., Broadhurst, T., Wong, J., et al. 2016, *MNRAS*, 459, 3447  
 Dunlop, J. S., McLure, R. J., Biggs, A. D., et al. 2017, *MNRAS*, 466, 861  
 Ebeling, H., Ma, C.-J., & Barrett, E. 2014, *ApJS*, 211, 21  
 Ellis, R. S., McLure, R. J., Dunlop, J. S., et al. 2013, *ApJL*, 763, L7  
 Ferrarese, L., Côté, P., Jordán, A., et al. 2006, *ApJS*, 164, 334  
 Finkelstein, S. L., Ryan, R. E. J., Papovich, C., et al. 2015, *ApJ*, 810, 71  
 Flewelling, H. A., Magnier, E. A., Chambers, K. C., et al. 2020, *ApJS*, 251, 7  
 Franco, M., Elbaz, D., Béthermin, M., et al. 2018, *A&A*, 620, A152  
 Fujimoto, S., Ouchi, M., Ono, Y., et al. 2016, *ApJS*, 222, 1  
 Fujimoto, S., Oguri, M., Brammer, G., et al. 2021, *ApJ*, 911, 99  
 Gaia Collaboration, Brown, A. G. A., Vallenari, A., et al. 2018, *A&A*, 616, A1  
 Gaia Collaboration, Prusti, T., de Bruijne, J. H. J., et al. 2016, *A&A*, 595, A1  
 Galametz, A., Grazian, A., Fontana, A., et al. 2013, *ApJS*, 206, 10  
 Gladders, M. D., López-Cruz, O., Yee, H. K. C., & Kodama, T. 1998, *ApJ*, 501, 571  
 Gladders, M. D., & Yee, H. K. C. 2000, *AJ*, 120, 2148  
 González, V., Labbé, I., Bouwens, R. J., et al. 2011, *ApJL*, 735, L34  
 González-López, J., Bauer, F. E., Romero-Cañizales, C., et al. 2017, *A&A*, 597, A41  
 Grillo, C., Karman, W., Suyu, S. H., et al. 2016, *ApJ*, 822, 78  
 Gruppioni, C., Béthermin, M., Loiacono, F., et al. 2020, *A&A*, 643, A8  
 Hack, W. J., Dencheva, N., Fruchter, A. S., et al. 2012, AAS Meeting, 220, 135.15  
 Hashimoto, T., Laporte, N., Mawatari, K., et al. 2018, *Natur*, 557, 392  
 Hatsukade, B., Ohta, K., Seko, A., Yabe, K., & Akiyama, M. 2013, *ApJL*, 769, L27  
 Hatsukade, B., Kohno, K., Umehata, H., et al. 2016, *PASJ*, 68, 36  
 Hildebrandt, H., Erben, T., Kuijken, K., et al. 2012, *MNRAS*, 421, 2355  
 Hoag, A., Bradač, M., Brammer, G., et al. 2018, *ApJ*, 854, 39  
 Hoaglin, D. C., Mosteller, F., & Tukey, J. W. 1983, *Understanding Robust and Exploratory Data Analysis* (New York: Wiley), 297  
 Hopkins, A. M., & Beacom, J. F. 2006, *ApJ*, 651, 142  
 Ilbert, O., McCracken, H. J., Le Fèvre, O., et al. 2013, *A&A*, 556, A55  
 Infante, L., Zheng, W., Laporte, N., et al. 2015, *ApJ*, 815, 18  
 Ishigaki, M., Kawamata, R., Ouchi, M., et al. 2015, *ApJ*, 799, 12  
 Jauzac, M., Clément, B., Limousin, M., et al. 2014, *MNRAS*, 443, 1549  
 Jiang, L., Kashikawa, N., Wang, S., et al. 2021, *NatAs*, 5, 256  
 Kaiser, N., Wilson, G., Luppino, G., et al. 1998, arXiv:astro-ph/9809268  
 Karman, W., Grillo, C., Balestra, I., et al. 2016, *A&A*, 585, A27  
 Kawamata, R., Ishigaki, M., Shimasaku, K., Oguri, M., & Ouchi, M. 2015, *ApJ*, 804, 103  
 Kokorev, V. I., Magdis, G. E., Davidzon, I., et al. 2021, *ApJ*, 921, 40  
 Labbé, I., Huang, J., Franx, M., et al. 2005, *ApJL*, 624, L81  
 Labbé, I., Oesch, P. A., Bouwens, R. J., et al. 2013, *ApJL*, 777, L19  
 Labbé, I., Oesch, P. A., Illingworth, G. D., et al. 2015, *ApJS*, 221, 23  
 Lagattuta, D. J., Richard, J., Clément, B., et al. 2017, *MNRAS*, 469, 3946  
 Le Floch, E., Papovich, C., Dole, H., et al. 2005, *ApJ*, 632, 169  
 Le Floch, E., Aussel, H., Ilbert, O., et al. 2009, *ApJ*, 703, 222  
 Limousin, M., Richard, J., Jullo, E., et al. 2016, *A&A*, 588, A99  
 Livermore, R. C., Finkelstein, S. L., & Lotz, J. M. 2017, *ApJ*, 835, 113  
 López-Cruz, O. 1997, PhD thesis, Univ. of Toronto  
 López-Cruz, O., Barkhouse, W. A., & Yee, H. K. C. 2004, *ApJ*, 614, 679  
 Lotz, J., Koekemoer, A., Coe, D., et al. 2019, Spitzer Frontier Fields, IPAC/IRSA, doi:10.26131/IRSA5  
 Lotz, J. M., Koekemoer, A., Coe, D., et al. 2017, *ApJ*, 837, 97  
 Lubin, L. M., Brunner, R., Metzger, M. R., Postman, M., & Oke, J. B. 2000, *ApJL*, 531, L5  
 Madau, P., & Dickinson, M. 2014, *ARA&A*, 52, 415  
 Mahler, G., Richard, J., Clément, B., et al. 2018, *MNRAS*, 473, 663  
 Manning, S. M., Casey, C. M., Zavala, J. A., et al. 2022, *ApJ*, 925, 23  
 McLeod, D. J., McLure, R. J., Dunlop, J. S., et al. 2015, *MNRAS*, 450, 3032  
 McLure, R. J., Dunlop, J. S., Bowler, R. A. A., et al. 2013, *MNRAS*, 432, 2696  
 Merlin, E., Fontana, A., Ferguson, H. C., et al. 2015, *A&A*, 582, A15  
 Merlin, E., Amorín, R., Castellano, M., et al. 2016a, *A&A*, 590, A30  
 Merlin, E., Bourne, N., Castellano, M., et al. 2016b, *A&A*, 595, A97  
 Molino, A., Benítez, N., Ascaso, B., et al. 2017, *MNRAS*, 470, 95  
 Muzzin, A., Marchesini, D., Stefanon, M., et al. 2013, *ApJ*, 777, 18  
 Oesch, P. A., Bouwens, R. J., Illingworth, G. D., et al. 2015, *ApJ*, 808, 104  
 Oesch, P. A., Bouwens, R. J., Illingworth, G. D., et al. 2013, *ApJ*, 773, 75  
 Oesch, P. A., Bouwens, R. J., Illingworth, G. D., et al. 2014, *ApJ*, 786, 108  
 Oesch, P. A., Brammer, G., van Dokkum, P. G., et al. 2016, *ApJ*, 819, 129  
 Oguri, M. 2010, *PASJ*, 62, 1017  
 Okabe, T., Oguri, M., Peirani, S., et al. 2020, *MNRAS*, 496, 2591  
 Oke, J. B. 1974, *ApJS*, 27, 21

- Ono, Y., Ouchi, M., Kurono, Y., & Momose, R. 2014, *ApJ*, 795, 5
- Oteo, I., Zwaan, M. A., Ivison, R. J., Smail, I., & Biggs, A. D. 2016, *ApJ*, 822, 36
- Owers, M. S., Randall, S. W., Nulsen, P. E. J., et al. 2011, *ApJ*, 728, 27
- Peng, C. Y., Ho, L. C., Impey, C. D., & Rix, H.-W. 2002, *AJ*, 124, 266
- Peng, C. Y., Ho, L. C., Impey, C. D., & Rix, H.-W. 2010, *AJ*, 139, 2097
- Postman, M., Coe, D., Benítez, N., et al. 2012, *ApJS*, 199, 25
- Rawle, T. D., Altieri, B., Egami, E., et al. 2016, *MNRAS*, 459, 1626
- Richard, J., Jauzac, M., Limousin, M., et al. 2014, *MNRAS*, 444, 268
- Richard, J., Claeysens, A., Lagattuta, D., et al. 2021, *A&A*, 646, A83
- Riess, A. G., Strolger, L.-G., Tonry, J., et al. 2004, *ApJ*, 607, 665
- Ryan, R. E. J., Gonzalez, A. H., Lemaux, B. C., et al. 2014, *ApJL*, 786, L4
- Salmon, B., Papovich, C., Finkelstein, S. L., et al. 2015, *ApJ*, 799, 183
- Schmidt, K. B., Treu, T., Brammer, G. B., et al. 2014, *ApJL*, 782, L36
- Sérsic, J. L. 1963, *BAAA*, 6, 41
- Shipley, H. V., Lange-Vagle, D., Marchesini, D., et al. 2018, *ApJS*, 235, 14
- Shu, X., Yang, L., Liu, D., et al. 2022, *ApJ*, 926, 155
- Skelton, R. E., Whitaker, K. E., Momcheva, I. G., et al. 2014, *ApJS*, 214, 24
- Smith, G. P., Ebeling, H., Limousin, M., et al. 2009, *ApJL*, 707, L163
- Steinhardt, C. L., Jauzac, M., Acebron, A., et al. 2020, *ApJS*, 247, 64
- Strait, V., Bradač, M., Coe, D., et al. 2020, *ApJ*, 888, 124
- Sun, F., Egami, E., Pérez-González, P. G., et al. 2021, *ApJ*, 922, 114
- Sun, F., Egami, E., Fujimoto, S., et al. 2022, *ApJ*, 932, 77
- Treu, T., Schmidt, K. B., Brammer, G. B., et al. 2015, *ApJ*, 812, 114
- Umehata, H., Smail, I., Swinbank, A. M., et al. 2020, *A&A*, 640, L8
- Wang, T., Elbaz, D., Schreiber, C., et al. 2016, *ApJ*, 816, 84
- Wang, T., Schreiber, C., Elbaz, D., et al. 2019, *Natur*, 572, 211
- Williams, R. J., Quadri, R. F., Franx, M., van Dokkum, P., & Labbé, I. 2009, *ApJ*, 691, 1879
- Wuyts, S., Labbé, I., Franx, M., et al. 2007, *ApJ*, 655, 51
- Yamaguchi, Y., Kohno, K., Hatsukade, B., et al. 2019, *ApJ*, 878, 73
- Yee, H. K. C., Gladders, M. D., & López-Cruz, O. 1999, in *ASP Conf. Ser.* 191, *Photometric Redshifts and the Detection of High Redshift Galaxies*, ed. R. Weymann et al. (San Francisco, CA: ASP), 166
- Zavala, J. A., Casey, C. M., Manning, S. M., et al. 2021, *ApJ*, 909, 165
- Zheng, W., Postman, M., Zitrin, A., et al. 2012, *Natur*, 489, 406
- Zhou, R., Newman, J. A., Mao, Y.-Y., et al. 2021, *MNRAS*, 501, 3309
- Zitrin, A., Meneghetti, M., Umetsu, K., et al. 2013, *ApJL*, 762, L30
- Zitrin, A., Zheng, W., Broadhurst, T., et al. 2014, *ApJL*, 793, L12
- Zitrin, A., Fabris, A., Merten, J., et al. 2015, *ApJ*, 801, 44